



1 **In situ apatite U-Pb, fission track and (U-Th)/He triple dating** 2 **using a simple embedding approach**

3

4 Christoph Glotzbach¹, Alexander Neely², Todd Alen Ehlers³

5

6 ¹ Department of Geosciences, University of Tuebingen, Germany

7 ² Arizona Geological Survey, Tucson, Arizona, USA

8 ³. School of Geographical and Earth Sciences, University of Glasgow, Scotland, UK

9

10 *Correspondence to:* C. Glotzbach (christoph.glotzbach@uni-tuebingen.de)

11

12 **Abstract.** Thermo- and geochronology techniques are foundational for many studies in tectonics, petrology, and
13 surface processes. They provide essential information about cooling histories during exhumation or burial, and
14 sediment provenance. Application of these methods has, in the past, primarily focused on applying individual
15 techniques to separate mineral grains. More recently, analytical developments in laser-ablation geochronology have
16 enabled the application of multiple dating techniques to an individual mineral grain (i.e., double or triple dating) to
17 provide enhanced resolution of the mineral's thermal history or dates and, therefore, the geologic or geomorphic
18 interpretations derived from it. However, applying multiple geochronological methods to individual grains often
19 requires methodological compromises that can restrict their applicability. In this study, we present a simplified and
20 robust technique for embedding apatite grains in Teflon mounts. This approach enables the combined application of
21 U-Pb, apatite fission track, and in-situ (U-Th)/He dating. In addition, this approach preserves the ability to quantify
22 trace-element compositions and radionuclide zoning. The approach enables to significantly increase the number of
23 measurements per sample, thereby opening the door to more robust results required for many applications.
24 To ensure high data quality from in-situ (U-Th)/He analyses, we introduce a decision matrix based on four key
25 evaluation criteria: laser pit shape, radionuclide zoning, grain geometry, and the pit–grain relationship. We apply this
26 integrated methodology to both the well-characterized Durango apatite standard and a sample from the crystalline
27 basement of the Odenwald, western Germany. Our results demonstrate the robustness and reliability of this approach.
28 Specifically, we obtain in-situ (U-Th)/He ages for Durango apatite (aliquot 1) of 31.04 ± 1.04 Ma (aliquot 1, n=35)
29 and 31.38 ± 2.53 Ma (aliquot 2, n=22), which are in excellent agreement with accepted reference ages. Apatite U-Pb
30 and fission track ages from the same grains, completing the triple dating approach, yield ages of 31.7 ± 1.9 Ma (U-Pb
31 concordia age) and 35.0 ± 4.4 Ma (central AFT age).
32 The Odenwald sample reveals a complex, multi-phase cooling history consistent with major regional geodynamic
33 events, including Late Cretaceous doming and Eocene exhumation associated with the formation of the Upper Rhine
34 Graben. Importantly, our results confirm that the Teflon mounting procedure, which requires short-term heating to
35 300°C, ~~did~~ does not cause measurable helium loss or reduce fission track density and track length in the near F-



36 endmember Durango apatite, a mineral susceptible to annealing. This supports the viability of this approach for high-
37 resolution, multi-system geo- and thermochronology thereby expanding the utility of these techniques to a broader
38 range of geoscience applications.

39

40

41 **1 Introduction**

42

43 Advancements in laser-based geochronological techniques over the past two decades have significantly expanded our
44 ability to extract complex time and thermal information from single mineral grains. These advancements have enabled
45 routine analysis of larger sample sizes to reduce sample uncertainties, increased the resolution of derived mineral
46 cooling histories, and to expand dating techniques to diverse detrital settings for sediment provenance determination.
47 In particular, the integration of multiple dating methods, commonly referred to as double or triple dating, offers the
48 opportunity to reconstruct the thermal evolution or provenance history of individual crystals with unprecedented
49 resolution. Such integrated approaches are especially powerful when applied to minerals like apatite and zircon, which
50 can retain distinct and complementary age information over a wide range of geological temperatures.

51 Recent progress in in-situ (U–Th)/He thermochronometry has demonstrated its compatibility with other dating
52 systems, such as U–Pb, Lu–Hf, and fission-track methods (e.g., Carrapa et al., 2009; Bedoya et al., 2024). These
53 developments not only enable us to refine thermal models and provenance interpretations but also address
54 longstanding analytical challenges, such as the detection and correction of parent-nuclide zonation within crystals.

55 Despite its promise, (U–Th)/He triple dating has so far been applied in a limited number of studies. Reiners et al.
56 (2005) were among the first to implement such an approach, combining external detector method (EDM) fission track
57 dating and LA-ICP-MS U–Pb analysis on detrital zircon. Following physical extraction from the mount, whole (or
58 better half) grain helium was measured and whole-grain (U–Th)/He dates calculated. Carrapa et al. (2009) extended
59 this strategy to apatite, embedding grains in epoxy for fission track and LA-ICP-MS U–Pb analysis, followed by
60 physical extraction and helium dating of entire crystals. Similarly, Danišik et al. (2012) and Zattin et al. (2012) used
61 variations of this workflow on detrital apatites. A more recent innovation by Bedoya et al. (2024) involved a sequential
62 analysis of Lu–Hf, U–Pb, and after polishing, the LA-ICP-MS-based fission track dating method was applied to single
63 apatite grains embedded in epoxy mounts.

64 Since epoxy degasses under ultra-high vacuum conditions, alternative embedding approaches have been investigated
65 to allow in situ (U–Th)/He dating (e.g. Boyce et al. 2006; Tripathy-Lang et al. 2013; Evans et al. 2015; Horne et al.
66 2016, 2019; Iwano et al. 2020). A complex two-mounting step procedure was introduced by Boyce et al. (2006),
67 mounting and polishing of grains in epoxy followed by physical removal of grains and pressing into non-degassing
68 indium with the polished surface facing down. Teflon was used for the embedding of zircons for in situ (U–Th)/He
69 dating by Tripathy-Lang et al. (2013). Similarly, it has been successfully used for zircon (U–Th)/He and U–Pb double
70 dating (e.g. Evans et al. 2015), while Kapton polyimide film can be used to keep grains in place during mounting. To
71 overcome issues associated with the low strength of Teflon, Pickering et al. (2020) introduced a new embedding



72 method based on Teflon-aluminium composite mounting. Low vapour-pressure epoxy (Torr Seal) was successfully
73 used for zircon, titanite and apatite in situ (U–Th)/He and U–Pb dating (Horne et al. 2016, 2019).
74 These studies collectively confirm the reliability of in-situ (U–Th)/He approaches for both age standards and detrital
75 samples (e.g., Boyce et al., 2006; Horne et al., 2016; Pickering et al., 2020; Tripathy-Lang et al., 2013). However, the
76 broader application of such methods remains limited due to practical challenges associated with the (U–Th)/He dating,
77 including the need to (i) produce flat and non-degassing mounts, (2) account for observed parent isotope zonation,
78 and (iii) properly model the diffusional effects in slowly cooled samples. Recent methodological advances have
79 addressed many of these issues. For example, a variation of in-situ He analysis enables direct evaluation of
80 radionuclide distribution, while improvements in thermal modelling now allow for accurate thermal history
81 reconstruction even of small or slowly cooled apatite/zircon grains (Glotzbach and Ehlers, 2024). In this study, we
82 present a new analytical workflow for in situ triple dating of apatite. Our method builds on previous approaches but
83 introduces key modifications to improve efficiency and reproducibility. Most notably, we employ a standardized
84 embedding protocol using a single Teflon foil, enabling three dating methods (U–Pb, (U–Th)/He, and fission track) to
85 be applied sequentially to the same grain without the need for removal or remounting of grains. This streamlined
86 technique provides a robust, high-throughput solution for simultaneously capturing crystallization and cooling
87 histories within single apatite and also zircon grains.

88

89

90 **2 Methods**

91

92 This section outlines the analytical procedures employed for conducting fission track, (U–Th)/He, and U–Pb triple
93 dating on apatite, as routinely performed at the University of Tuebingen, Germany. The methods presented here follow
94 an integrated workflow optimized for consistency and reproducibility across all three dating techniques. We provide
95 a comprehensive description of each step, including sample mounting, apatite grain selection, fission track counting,
96 helium measurement, pit volume determination, trace element measurement and required data reduction to calculate
97 fission track, (U–Th)/He, and U–Pb dates.

98

99 **2.1 Mount preparation**

100

101 In this study, we applied a mounting procedure using 0.5 mm Teflon film (PFA FlonFilm™ 600), commonly employed
102 for zircon FT analysis, to embed apatite grains. This approach provides compatibility with all three dating techniques,
103 including FT visibility, ultra-high vacuum (UHV) stability, and flatness for LA analyses. The preparation steps were
104 as follows:

- 105 1. **Initial Setup:** A clean glass slide was coated with a thin film of epoxy to fix grains in place during mounting.
- 106 2. **Bead Placement:** At least three ~150 µm diameter glass beads were arranged in a triangular formation 5–8
107 mm apart. These served as grinding references to ensure that more than one mean alpha-particle-stopping
108 distance (~20 µm) was removed during polishing (following Pickering et al., 2020). Moreover, their circular



109 geometry makes them clearly distinguishable on the mount and facilitates the automated repositioning of
110 selected grains when transferring between analytical setups.

111 3. **Grain Distribution:** A few hundred apatite grains were placed within a ~2.54 cm diameter area around and
112 between the glass beads.

113 4. **Teflon Film Application:** A 2.54 cm diameter Teflon disc was placed over the grains.

114 5. **Mount Sealing:** A second glass slide was laid atop the Teflon film. The assembly was then heated to 295°C
115 and pressed to embed the grains into the Teflon. Temperatures were independently measured with a Voltcraft
116 TP-206 surface probe with a temperature accuracy of 2.5°C connected to a Voltcraft IR 800-20C
117 thermometer. Two methods were used for the heating:

118 ○ **Heat Plate Method:** The upper glass was preheated separately, while the lower slide with grains
119 and Teflon was heated for ~1 minute before applying the top slide and manually pressing for ~30
120 sec until the Teflon slightly expanded.

121 ○ **Heat Press Method:** The glass–Teflon–glass sandwich was heated in a press. After ~1 minute,
122 pressure was applied until the Teflon slightly expanded around the grains.

123 Both methods provided similar results. Note that the exact mounting temperature and time required before
124 the mount is pressed depend on the material properties and the thickness of the used glass slides and Teflon
125 film. See Sect. 6 for modelled time-temperature paths and the potential effect on He diffusion and fission
126 track annealing.

127 6. **Cooling:** The slides were removed from the heat source and allowed to cool while maintaining pressure on
128 the upper glass. This step ensured a flat Teflon surface, which is essential for subsequent grinding, polishing,
129 and laser-based analyses.

130

131 2.2 Modelling mounting-induced annealing and diffusion

132 The embedding method applied here using Teflon film requires heating the Teflon and mineral grains to temperatures
133 close to 300°C, clearly exceeding the temperature at which He diffusion and fission track annealing in apatite is
134 significant over geological timescales (e.g. Ketcham et al. 1999; Farley 2000). We therefore evaluated the effect of
135 the mounting using two different approaches: (i) forward thermal modelling of the effect of short-term heating on He
136 diffusion and fission track annealing, and (ii) comparing fission track length distributions of samples mounted with
137 epoxy (without heating) and Teflon (heating).

138 We implemented a finite difference model to simulate 1D heat conduction. The thermal parameters, initial
139 temperatures, and boundary conditions are listed in Table 1. Note that the hotplate temperature required to lower the
140 Teflon viscosity depends on the type of Teflon and the thickness of the glass slides. The PFA FlonFilm 600 used has
141 a melting point of 302-310°C and is dimensionally stable until 260°C, whereas it becomes soft enough for grains to



142 penetrate into the film at ~290°C. We set the temperature of the hot plate to 295°C and controlled it with a
143 thermocouple strip sensor with an accuracy of 2.5°C.

144

145 Table 1: Thermal parameters of 1D thermal model of the mounting process.

146

Parameter	Value
Hot plate temperature (°C)	295
Ambient temperature (°C)	20
Spatial resolution (mm)	0.05
Glass thermal diffusivity (m ² /s)	4.80E-07
Glass thickness (mm)	2 or 3
Teflon thermal diffusivity (m ² /s)	7.74E-08
Teflon thickness (mm)	0.5

147

148 **2.3 Grinding and polishing**

149 After embedding, the Teflon film was ground down by at least 20 µm using progressively finer abrasive papers (P800
150 – 22 µm, P1200 – 13 µm, P2500 – 8 µm). Final polishing was conducted on a semi-automatic polishing machine using
151 6 µm, 3 µm, and 1 µm diamond suspensions, yielding a smooth and flat surface suitable for optical and laser-based
152 dating methods.

153

154 **2.4 Fission track etching**

155

156 Prior to etching, sample mounts were cleaned with ethanol and compressed air to remove surface contaminants.
157 Etching followed the protocol of Donelick et al. (2005). A glass beaker was filled with 5.5 M HNO₃ and heated to
158 21°C. Two mounts were held with PFA tweezers, polished surfaces facing outward, and immersed in the acid for 20
159 seconds. Immediately after etching, mounts were transferred to deionized water to halt the reaction.

160

161

162 **2.5 Grain selection**

163 Grain selection was conducted using a Zeiss Axio Imager Z2m microscope equipped with a custom Python macro,
164 available from the associated Zenodo repository (<https://doi.org/10.5281/zenodo.18979745>) to streamline and



165 standardize the process. The procedure consists of several sequential steps to ensure the selection of suitable grains
166 for in-situ (U-Th)/He, fission track and U-Pb dating:

- 167 1. **Sample Imaging:** The entire grain mount was imaged using the 10× objective under reflected light. A
168 stitching routine was applied to create a high-resolution overview image of the full mount, enabling efficient
169 navigation and documentation.
- 170 2. **Reference Point Definition:** Three easily recognizable glass beads embedded in the mount were selected to
171 form a roughly equiangular triangle. These served as spatial reference points for accurate sample navigation
172 and alignment during subsequent analyses.
- 173 3. **Grain Inspection:** Using the stitched overview image as a guide, individual grains were inspected at higher
174 magnification (100× objective) under transmitted light. This allowed a detailed evaluation of each grain's
175 geometric, surface and optical characteristics.
- 176 4. **Grain Marking:** Following inspection, grains were marked directly on the stitched overview image. Grains
177 that met the selection criteria were marked in green, while those that failed were marked in yellow. This
178 visual tracking system ensured that no grain was inadvertently evaluated more than once.
- 179 5. **Grain Imaging:** Suitable grains were imaged using both reflected and transmitted light to document their
180 morphology and internal features. The vertical elevation of the polished grain surface was first identified and
181 marked. This reference point was then used to capture (i) a high-resolution reflected light image of the grain
182 surface, (ii) a transmitted light image stack covering the top 20 μm of the grain, and (iii) a low-resolution
183 image with a burned-in circle marking the envisaged ablation spot. These image datasets serve two essential
184 purposes: they are used for off-line fission track counting and enable subsequent visual inspection of the
185 analyzed grain even after destructive laser ablation.
- 186 6. **Grain Coordinate Export:** Once >20 grains were marked as suitable for subsequent analyses, the
187 coordinates of those grains together with reference point coordinates were exported as text files to be
188 imported later in the excimer laser software.

189 The applied grain selection criteria focused on aspects such as grain size, geometry, surface quality, and purity (e.g.,
190 Flowers et al., 2023). Grains with favorable shapes (ideally euhedral) and low surface roughness were selected.
191 Sufficient size was required to accommodate the ablation pit used in LA-MS analysis. In addition, grains were
192 screened for inclusions, cracks, and other imperfections that could compromise dating accuracy. Note that the c-axis
193 orientation of selected grains was not a determining selection criterion, but only those grains with a c-axis parallel to
194 the polished grain surface were used for fission track dating.

195

196 2.6 Fission track counting

197



198 Fission track dating was performed using a custom-programmed MATLAB App
199 (<https://doi.org/10.5281/zenodo.18979745>) designed to streamline and enhance the efficiency of track counting. The
200 app enables a seamless transition between the reflected light image and the transmitted light image stack, allowing
201 clear visualization of individual etched tracks. It also provides a visual control system to track which fission tracks
202 have already been counted, minimizing the risk of duplicate or missed counts. Additionally, the app includes a tool to
203 measure the diameter of etched tracks parallel to the c-axis (Dpar), with all counting statistics and Dpar values
204 automatically stored in a structured table for further analysis and modeling.

205
206

207 **2.7 He measurement**

208

209 In-situ helium measurements on apatite grains were performed using a RESOchron system from Applied Spectra,
210 which integrates an Alphachron He-line with a RESOLUTION SE 193 nm excimer laser. Samples were mounted in
211 a UHV cell, which was pumped overnight to pressures below 1×10^{-8} torr. A low-resolution image stack of the mount
212 was captured to relocate reference glass beads and recalculate laser pit positions, accounting for any positional shifts.
213 The latter might occur since Teflon (PTFE) does have a high thermal expansion coefficient of $\sim 115 \times 10^{-6} \text{ K}^{-1}$ and the
214 mount temperature might vary between rooms or instruments during grain selection and He measurement. A $1 \text{ }^\circ\text{C}$
215 temperature change could cause a $\sim 3 \text{ }\mu\text{m}$ expansion across the 1" mount, so the temperature around the UHV cell was
216 stabilized to near $21 \text{ }^\circ\text{C}$ using a Peltier-based air-air control system. Prior to ablation, each laser pit position was
217 compared with the planned position (based on a low-resolution image, see Sect. 2.5) and adjusted if necessary. Helium
218 was extracted using laser parameters of 20–50 μm spot size, 1.3–3 J/cm^2 fluence, 10 Hz repetition rate, and 2–8
219 seconds ablation time. Laser fluences of 1.3, 2.0 and 3.0 J/cm^2 removed 0.075, 0.100 and 0.125 $\mu\text{m}/\text{shot}$, resulting
220 in pan-cake-shaped pits of 1–10 μm depth. The released ^4He was mixed with a known amount of ^3He , purified with a
221 cold getter, and measured using a Pfeiffer PrismaPlus mass spectrometer. The measurement sequence included two
222 Q-shots, multiple lineblanks, and up to five samples between blank checks. Initially, four lineblanks were run after
223 two Q-shots due to their high ^4He yield (\sim four orders of magnitude higher than samples). Lineblank levels were
224 monitored and measured in-between samples. The lineblank contained, on average $0.00441 \pm 0.00008 \text{ ncc } ^4\text{He}$.
225 The limit of detection (three times the standard deviation) was as low as $0.00024 \text{ ncc } ^4\text{He}$, enabling accurate dating of
226 apatites as young as 2 million years, assuming 30 ppm eU and pit dimensions of 50 μm diameter \times 5 μm depth.

227
228

229 **2.8 Pit Volume Estimation**

230

231 To convert the measured He amounts into concentrations, an accurate determination of the laser pit volumes is
232 required. Following He analysis, the sample mount is removed from the UHV cell and transferred to a Zeiss Axio
233 Imager Z2m microscope equipped with a Zeiss LSM900 confocal laser system. A custom Python script
234 (<https://doi.org/10.5281/zenodo.18979745>) automates the volume estimation process through a series of steps:



- 235 1. **Sample Imaging:** The entire grain mount is imaged using a 10× objective under reflected light. A stitching
236 routine generates a high-resolution overview image, enabling precise navigation and documentation.
- 237 2. **Reference Point Definition:** The three reference glass beads are marked to recalculate the coordinates of
238 previously selected grains and their associated laser pits.
- 239 3. **Z-Stack Limit Definition:** For each pit, the upper and lower z-coordinates are adjusted using confocal laser
240 scanning with the pinhole set to 1 Airy unit, ensuring accurate focus on the grain surface and pit bottom.
- 241 4. **Z-Stack Imaging:** After defining z-limits for all pits, z-stack images are collected using a 100×
242 objective with a depth resolution of ~0.1 μm. Additionally, a 20× reflected light image is taken for each grain
243 to document pit geometry and measure distances between the laser pit and grain edges required for thermal-
244 history modelling.
- 245 5. **Pit Volume Measurement:** Using ConfoMap (Zeiss) software, pit volumes are extracted from the z-stacks.
246 A macro automates this by first correcting for any tilt, defining the original grain surface, and subtracting the
247 pit surface from the interpolated pre-ablation surface to yield the net pit volume.
- 248 6. **Helium Concentration Calculation:** The He amount measured from the ablation is then divided by the
249 corresponding pit volume to derive the He concentration (e.g., in at/μm³).

250
251 This methodology ensures precise and consistent volume estimations critical for high-resolution in-situ (U-Th)/He
252 dating.

253 254 255 **2.9 Trace Element Measurement**

256
257 Trace element concentrations in apatite were measured using a LA-ICP-MS system consisting of a RESolution SE
258 193 nm excimer laser coupled to an Agilent 7900 ICP-MS. Samples, NIST SRM612 trace element reference glass and
259 apatite standards Durango and McClure Mountain Syenite are placed within a Laurin Technic S155 dual-volume
260 ablation cell. To correct for instrumental drift and elemental fractionation during ablation, a sample bracketing
261 approach was employed following the protocol of Paton et al. (2010). The trace elements analyzed included ²⁹Si, ³¹P,
262 ³⁵Cl, ⁴³Ca, ⁴⁴Ca, ⁵⁵Mn, ⁸⁸Sr, ⁸⁹Y, ¹³⁹La, ¹⁴⁰Ce, ¹⁴¹Pr, ¹⁴⁶Nd, ¹⁴⁷Sm, ¹⁵³Eu, ¹⁵⁷Gd, ¹⁵⁹Tb, ¹⁶³Dy, ¹⁶⁵Ho, ¹⁶⁶Er, ¹⁶⁹Tm, ¹⁷²Yb,
263 ¹⁷⁵Lu, ²⁰²Hg, ²⁰⁴Hg, ²⁰⁶Pb, ²⁰⁷Pb, ²⁰⁸Pb, ²³²Th and ²³⁸U. Before measurement, the ICP-MS was tuned using the SRM612
264 glass to optimize for high sensitivity of ²⁰⁶Pb, ²³²Th, and ²³⁸U, and in addition, targeting a ²³²Th/²³⁸U ratio of 1. The cell
265 gas configuration included 350 mL/min He, 850 mL/min Ar, and a minor 0.5 mL/min N₂ addition, providing efficient
266 aerosol transport and signal stability.

267 In line with Evans et al. (2015), ablation was performed with a second laser shot (nested pit) placed at the center of
268 the original He analysis pit to maintain consistent sampling conditions. To ensure comparability between glass,
269 standards, and unknowns, the nested pit had a smaller diameter of 24 or 30 μm, depending on whether the original pit
270 was 30 or 50 μm in diameter, ensuring ablation occurred on a flat surface.



271 Each analysis began with a 20-second gas background followed by 30 seconds of ablation at a fluence of 3 J/cm². The
272 resulting data were processed using an in-house MATLAB App (<https://doi.org/10.5281/zenodo.18979745>), which
273 carried out:

- 274 • Automatic removal of data gaps
- 275 • Manual or automatic outlier rejection based on a running standard deviation threshold
- 276 • Background subtraction
- 277 • Manual or automated selection of integration intervals
- 278 • Calculation of trace element concentrations using ⁴³Ca (or ⁴⁴Ca) as the internal standard

279 Assumed CaO concentrations were 11.9% for SRM612 (Jochum et al., 2011) and 55.6% for apatite, based on its
280 stoichiometric composition. Calibration curves were interpolated between 5-6 subsequent SRM612 measurements to
281 account for temporal drift. Final concentrations were calculated following the method of Longerich et al. (1996).

282

283

284 **2.10 Fission track age calculation**

285

286 Fission-track ages were calculated using the ζ -based LA-ICP-MS approach (Donelick et al. 2005) with Durango
287 apatite as the primary age standard. Kinetic properties of apatite crystals were determined by measurement of Dpar
288 values (mean of 4 per crystal), complemented by chlorine measurements using LA-ICP-MS and Durango apatite for
289 calibration (e.g. Chew et al. 2013).

290 Repeated measurements of 20 Durango shards measured during 15 different LA-ICP-MS sessions with in total 72
291 individual measurements yield a zeta (ζ) of 2479±33 calculated with:

292

$$293 \quad \zeta = \frac{e^{\lambda_d t_{std}} - 1}{\lambda_d \rho_s / U} \quad \text{Eq. 1}$$

294

295 where λ_d is the total decay constant of ²³⁸U [1/Myr], t_{std} is the age of Durango apatite of 31.44±0.18 Ma (McDowell
296 et al. 2005), ρ_s is the spontaneous fission track density [tracks/cm²] and U is the Uranium concentration [g/g].

297

298

299 **2.11 U-Pb age calculation**

300

301 U-Pb age calculations were performed using the in-house MATLAB App (<https://doi.org/10.5281/zenodo.18979745>).

302 Raw isotope ratios, such as ²⁰⁶Pb/²³⁸U were corrected for drift in mass ratios and downhole fractionation following the
303 approach of Paton et al. (2010) by employing age standards - Durango apatite and 91500 zircon. Common lead
304 corrections were carried out either by directly measuring ²⁰⁴Pb in zircon or, in cases where ²⁰⁴Pb counts were
305 significant and indistinguishable from the background (as in apatite), a ²⁰⁷Pb or ²⁰⁸Pb correction following Williams
306 (1998) was applied. This method relies on a common lead evolution model, for which we used the Stacey and Kramers
307 (1975) model. Final sample ages were derived from either a Tera-Wasserburg diagram or following the common lead



308 correction derived from a Concordia plot. It is important to note that prior chemical etching of fission tracks may
309 affect U–Pb dating by removing material and thereby lowering grain density, particularly at the surface and in areas
310 with high spontaneous fission track densities. However, the majority of etched tracks were removed during the first
311 ablation step for He measurement, and Abdullin et al. (2021) demonstrated that U–Pb dating is not significantly
312 influenced by prior etching.

313

314

315 **3 Sample Details**

316

317 We applied the triple dating approach to a Durango apatite standard and a sample from the basement of the Odenwald,
318 Germany (22BGE055T). Two Durango aliquots with 35 (Durango1) and 25 (Durango2) crystal shards, and 22 grains
319 from 22BGE055T were analysed. The Durango apatite comes from the skarn deposit of the Cerro de Mercado iron
320 mine in Durango, Mexico. Apatites formed in a high-temperature hydrothermal environment linked to the eruption of
321 intermediate to felsic ignimbrites sourced from the Chupaderos caldera (e.g. McDowell et al. 2005). While the
322 Durango apatite is a challenging standard for U–Pb dating due to its young age, high Th/U ratio, and variable common
323 lead composition, it is nonetheless widely used as a primary age standard for fission track and (U–Th)/He dating. ID-
324 TIMS apatite U–Pb analyses yielded an age of 32.716 ± 0.061 Ma, although this likely overestimates the true
325 crystallization age due to excess ^{206}Pb (Paul et al. 2021). The latter is mostly the product of the ^{238}U decay chain, but
326 can also be produced in a small amount from ^{230}Th directly, which is incorporated in minerals with a high Th/U ratio,
327 such as Durango apatite (Paul et al. 2021). Therefore, we assume that the indirect $^{40}\text{Ar}/^{39}\text{Ar}$ dates of the
328 stratigraphically bracketing ignimbrite (31.44 ± 0.18 Ma; McDowell et al. 2005) more reliably reflect the
329 crystallization age of Durango apatite. Since the Durango apatite formed near the surface, we expect that our triple
330 dating approach will yield very similar ages. Analyses were conducted on 100–200 μm shards of a crushed gem-quality
331 Durango apatite crystal.

332 Sample 22BGE055T was collected from the crystalline basement of the Odenwald, which, along with the Black Forest,
333 forms the uplifted eastern shoulder of the Upper Rhine Graben. This sample was taken at latitude 49.57254°N and
334 longitude 8.66981°E north of Weinheim, Germany, from the Lower Carboniferous Weschnitz pluton, and is
335 granodioritic in composition. Previous K–Ar dating on biotite and hornblende yielded ages of 320–330 Ma (Kreuzer
336 and Harre 1975), and petrographic analyses reveal a predominantly mantle derived source of melts (e.g. Will et al.
337 2021). Following the emplacement at pressures of 4.5–5 kbar and depths exceeding 15 km (Stein and Dietl 2001), the
338 crystalline basement was largely levelled and exposed to Earth’s surface prior to the Upper Permian marine
339 transgression. Subsequent subsidence continued at least until the Middle Jurassic, accompanied by deposition of up
340 to 1500 m of various sedimentary rocks (Wagner 1969). Large-scale doming resulted in complete removal of the
341 sedimentary cover in the northern Odenwald during Eocene times, which is recorded in the buried Upper Rhine graben
342 Eocene planation surface (Ziegler 1990) The southern Odenwald remained partly buried, as evidenced by the
343 emplacement of the Katzenbuckel at ~ 68 –70 Ma (Schmitt et al. 2007) into Middle Jurassic rocks (Wagner 1969). Final
344 exhumation of the southern Odenwald likely initiated during the Middle Oligocene, driven by tectonic activity along



345 the Upper Rhine Graben (Wagner 1969). Grain selection mostly followed the above criteria (Sect. 2.5), however,
346 some subhedral grains were selected that were suitable for U-Pb and AFT dating, but not ideal for (U-Th)/He dating.
347 In total 22 grains with grain radii from 32 to 128 μm were analysed.

348

349

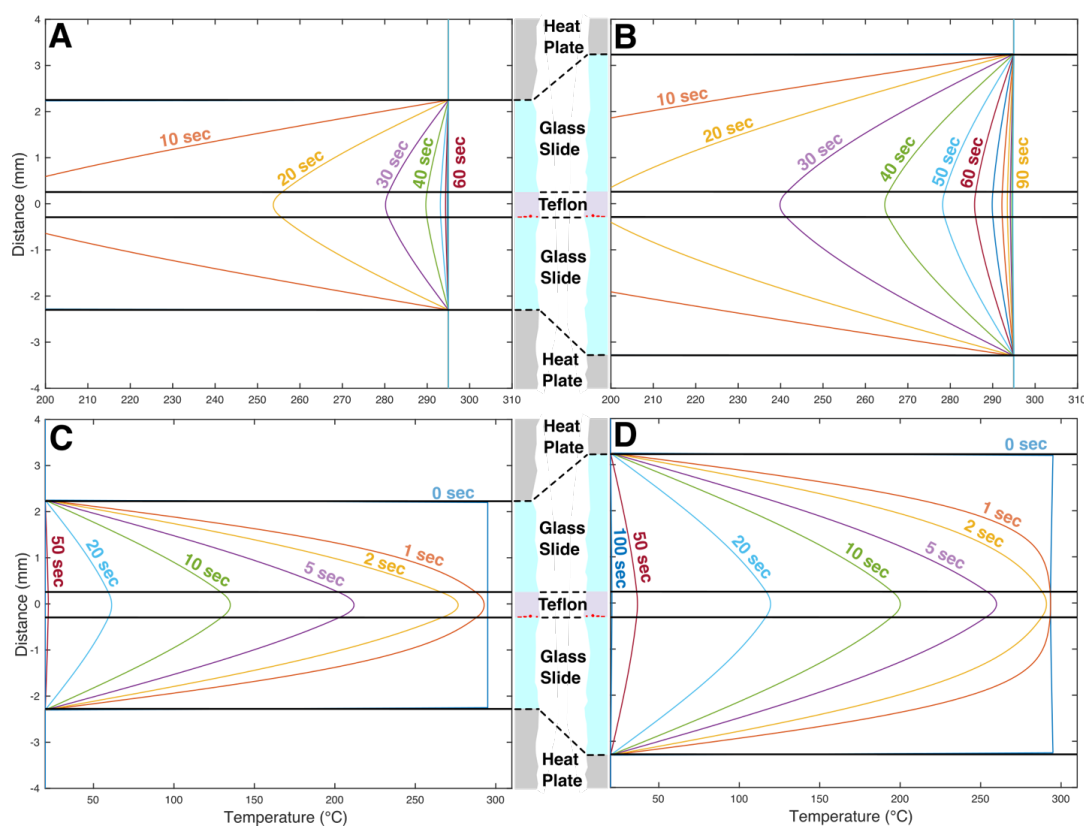
350 4 Results

351

352 4.1 Mounting induced annealing and diffusion

353

354 Our modelling approach to quantify the annealing of fission tracks and diffusion of He in apatite neglects that grains
355 do have a higher thermal diffusivity compared to the surrounding Teflon film and that initially apatite grains reside
356 between the glass slide and Teflon film for some time. We do, however, expect that this is only marginally impacts
357 the resulting thermal evolution. The 1D thermal diffusion modelling revealed that the Teflon film approached the hot
358 plate temperature after 60 sec for 2 mm thick glass slides, whereas it took 90 sec for 3 mm thick glass slides (Fig.
359 1A,B). Cooling to ambient temperature is comparable assuming efficient heat transfer (ventilation) from the glass
360 slides (Fig. 1C,D).



361



362 Figure 1: Temperature evolution with 2 mm and 3 mm glass slides during the mounting process. A/B) Heating phase
363 of the glass–Teflon–glass sandwich on top of the heat plate. C/D) Cooling phase of the glass–Teflon–glass sandwich
364 after removal from the heat plate.

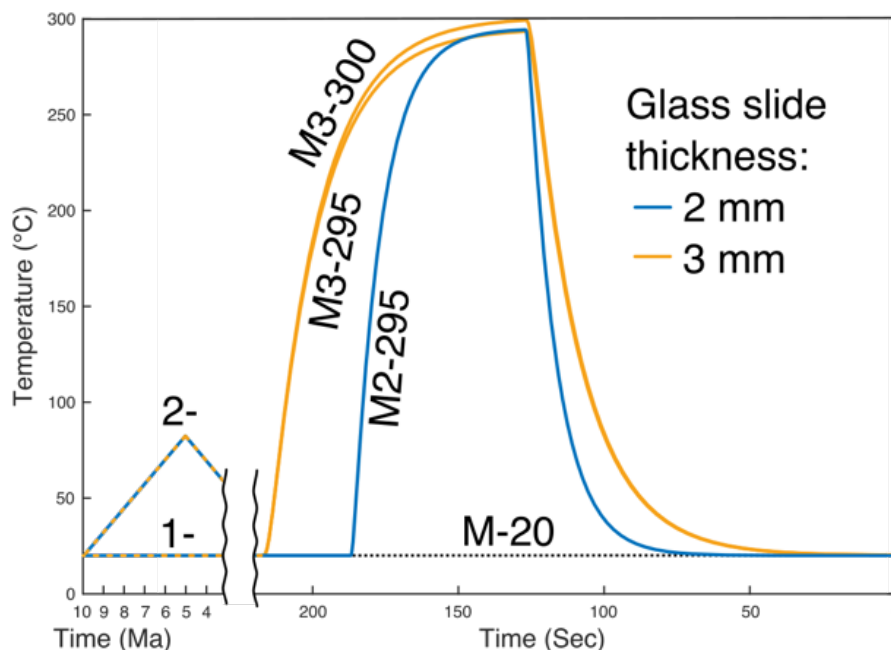
365

366 The modelled time-temperature (tT) paths at the locations of the embedded apatite grains (tiny red dots in Fig. 1) on
367 the lower side of the Teflon film were extracted from the model and used as input for forward thermal modelling of
368 apatite fission-track and (U-Th)/He data. Since fission track annealing is length-dependent and the track stability
369 against annealing increases as tracks become shorter we tested two scenarios without (1-) and with (2-) pre-mounting
370 track shortening (Fig. 2). Both scenarios assume that the temperature of the theoretical apatite grain was 20°C at 10
371 Ma and heating during mounting occurred at 3-4 minutes before the end of the model to allow cooling to room
372 temperature (Fig. 2). Scenarios 1- assumes that the pre-mounting temperature stayed at 20°C, while linear heating and
373 cooling to 80°C at 5 Ma was used in scenarios 2- to reduce track length before mounting (Fig. 2). These pre-mounting
374 tT paths were combined with modelled mounting tT paths for 2 (M2) and 3 mm (M3) thick mounting glasses and
375 mounting temperatures of 295 to 320°C (Fig. 2).

376

377

378



379 Figure 2: Time-temperature (tT) path used to model the impact of our mounting protocol on apatite fission track
 380 annealing and He diffusion. Model scenarios include no pre-mounting heating (1-) and linear heating to 80°C at 5 Ma
 381 (2-), followed by mounting tT paths for glass thicknesses of 2 and 3 mm (M2, M3) and hot plate/press temperatures
 382 of 295 to 320°C. For comparison an unrealistic mounting temperature of 20°C is assumed (scenarios M-20).

383
 384 During mounting, the modelled temperature briefly matches the hot plate temperature, remaining above 250°C for
 385 approximately 45 seconds with 2 mm glass and about 60 seconds with 3 mm glass. This results in minor apatite fission
 386 track annealing and negligible helium diffusion for Durango-type apatite chemistry (Table 2). Without pre-mounting
 387 fission-track annealing (scenario 1-), AFT ages are about 1% younger at a mounting temperature of 295°C than in
 388 unmounted samples. This discrepancy increases to 2% at 305°C and exceeds 3.6% at 320°C. The length reduction of
 389 unannealed fission tracks is, on average, less than 0.1 μm - at the threshold of detectability - and does not significantly
 390 affect modelled cooling histories. Similarly, apatite (U-Th)/He ages are negligibly affected by the mounting process
 391 (Table 2).

392 In Scenario 2, where pre-mounting heating causes partial fission-track annealing, subsequent mounting at
 393 temperatures below 310°C results in less than 0.5% additional fission-track annealing and less than 0.7% He diffusion.
 394 Notably, the mean track length (MTL) remains virtually unchanged for mounting temperatures below 305°C. These



395 findings indicate that the Teflon-based mounting procedure has no significant impact on apatite fission-track or (U-
396 Th)/He data when mounting is performed quickly and at temperatures not exceeding ~300°C.

397

398

399 Table 2: Modelled apatite fission track (AFT) age, mean track length (MTL), (U-Th)/He (AHe) age and total He for
400 various (pre-) mounting scenarios for Durango-type apatite chemistry and annealing and diffusion models of Ketcham
401 et al. (2007) and Flowers et al. (2009).

Scenario	Hot Plate Temp (°C)	AFT age (Ma)	MTL (µm)	AHe age (Ma)	Total He (mol/g)
1-M-20	20	10.20	14.54±1.05	9.90	0.8824
1-M2-295	295	10.10	14.47±1.04	9.90	0.8819
1-M3-295	295	10.10	14.46±1.04	9.90	0.8818
1-M3-300	300	10.10	14.45±1.04	9.90	0.8817
1-M3-305	305	10.00	14.38±1.04	9.89	0.8814
1-M3-310	310	9.97	14.32±1.04	9.89	0.8812
1-M3-320	320	9.83	14.16±1.04	9.88	0.8805
2-M-20	20	9.01	13.27±1.43	6.13	0.5460
2-M2-295	295	9.01	13.26±1.41	6.13	0.5459
2-M3-295	295	9.00	13.26±1.40	6.13	0.5458
2-M3-300	300	9.00	13.25±1.39	6.13	0.5458
2-M3-305	305	8.98	13.22±1.38	6.09	0.5428
2-M3-310	310	8.96	13.20±1.37	6.09	0.5427
2-M3-320	320	8.92	13.15±1.33	6.09	0.5426

402

403 To support the modelling approach, an experiment was conducted using the same sample mounted in two different
404 ways: in epoxy without heating and in Teflon with heating. Fission track length measurements were then performed.
405 The sample used was from the Upper Triassic Stubensandstein formation in southwestern Germany (sample
406 22BGE032T), sharing a similar cooling history as sample 22BGE055T.

407 In the epoxy-mounted sample, 103 confined fission tracks were measured, yielding a relatively broad track length
408 distribution with a c-axis corrected mean track length (MTL) of $13.12 \pm 1.34 \mu\text{m}$. In the Teflon-mounted sample, also
409 with 103 measured tracks, the MTL was $13.09 \pm 1.05 \mu\text{m}$. These results support the modelling outcome, confirming
410 that the Teflon mounting protocol leads to negligible shortening of apatite fission tracks.

411

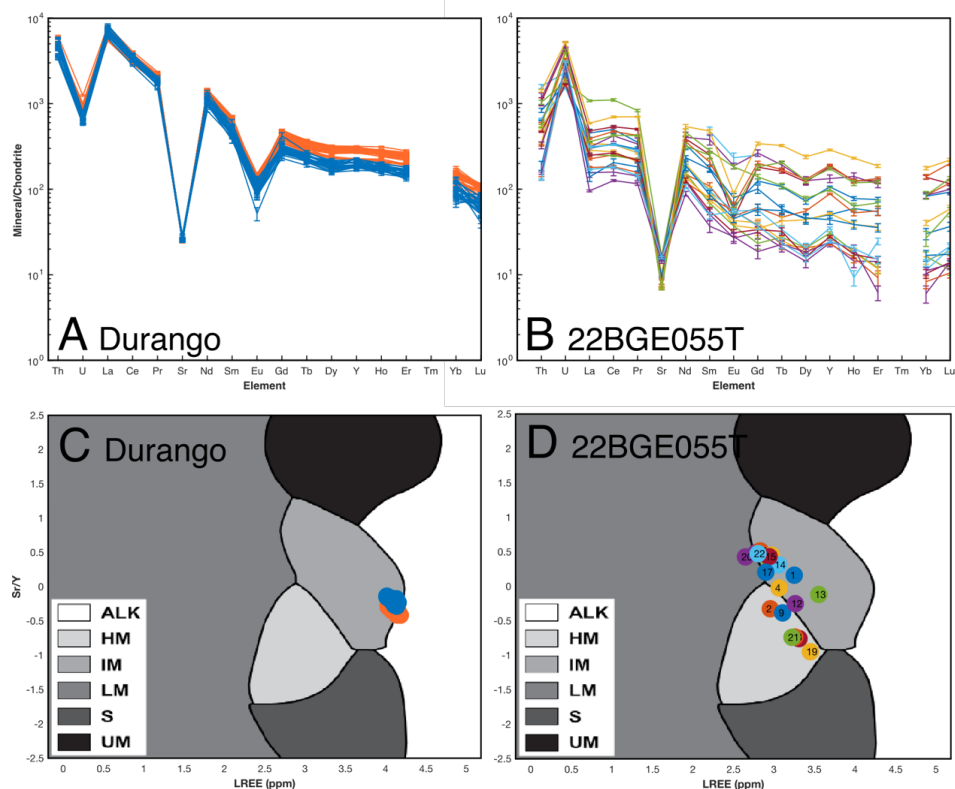
412

413 4.2 Trace Element Composition

414



415 The trace element composition of Durango apatite is characterized by distinctly elevated light rare earth element
416 (LREE) concentrations relative to heavy rare earth elements (HREE), a pronounced negative Eu anomaly, and high
417 Th/U ratios (Fig. 3A). According to the classification scheme of O'Sullivan et al. (2020), these characteristics would
418 suggest a source in mafic I-type granitoids (IM) (Fig. 3C). However, this classification likely oversimplifies the
419 complex volcanic environment in which Durango apatite crystallized, and misclassification is probable given the non-
420 igneous (hydrothermal) processes involved. Slight compositional differences observed between the Durango1 and
421 Durango2 aliquots are attributed to moderate zoning, as is common in Durango apatite (e.g. Chew et al. 2016).
422 In contrast, apatite grains from sample 22BGE055T display a broader compositional range, particularly in HREE
423 concentrations, which vary by more than an order of magnitude (Fig. 3B). These grains show consistently low Th/U
424 ratios and are marked by a significant negative Sr anomaly. Most grains exhibit only moderately higher LREE ratios
425 relative to HREE, and four grains stand out with a strong negative Eu anomaly, these same grains also record the most
426 pronounced Sr depletion. The presence or absence of a Eu anomaly is interpreted to reflect the timing of feldspar
427 crystallization relative to apatite. Eu exist in two oxidation states (2+ and 3+) in magmatic systems and Eu²⁺ is similar
428 in charge and has a quite similar ionic radius to Ca²⁺, and is therefore largely removed from the melt through
429 crystallisation of feldspar (e.g. Holder et al. 2020). Apatite crystallizing after feldspar will therefore record a negative
430 Eu anomaly, whereas early-crystallizing apatite typically lacks this feature (e.g. Larsen 2002). Classification based on
431 REE spider diagram patterns (Fig. 3D) suggests that the apatites in sample 22BGE055T most likely originate from I-
432 type granitoids and high-grade metamorphic rocks, consistent with a dominantly mantle-derived I-type magmatic
433 source (e.g. Will et al. 2021).



434

435 Figure 3: A,B) Chondrite-normalised rare earth element (REE) plus U, Th and Sr multi-element plot (spider diagram)
 436 of Durango apatite (red – Durango1, blue – Durango2) and sample 22BGE055T. Gaps represent non-analysed
 437 elements. C,D) Sr/Y vs. Σ LREE biplot of Durango apatite (red – Durango1, blue – Durango2) and 22BGE055T trace
 438 element results. Background grey colours represent the classification proposed O’Sullivan et al. (2020): ALK – alkali-
 439 rich igneous, HM – partial-melts/leucomes/high-grade metamorphic, IM – mafic I-type granitoids and mafic igneous,
 440 LM – low- and medium-grade metamorphic and metasomatic, S – S-type granitoids and high-aluminum saturation
 441 index felsic I-types, UM – ultramafic rocks including carbonatites, lherzolites and pyroxenites.

442

443

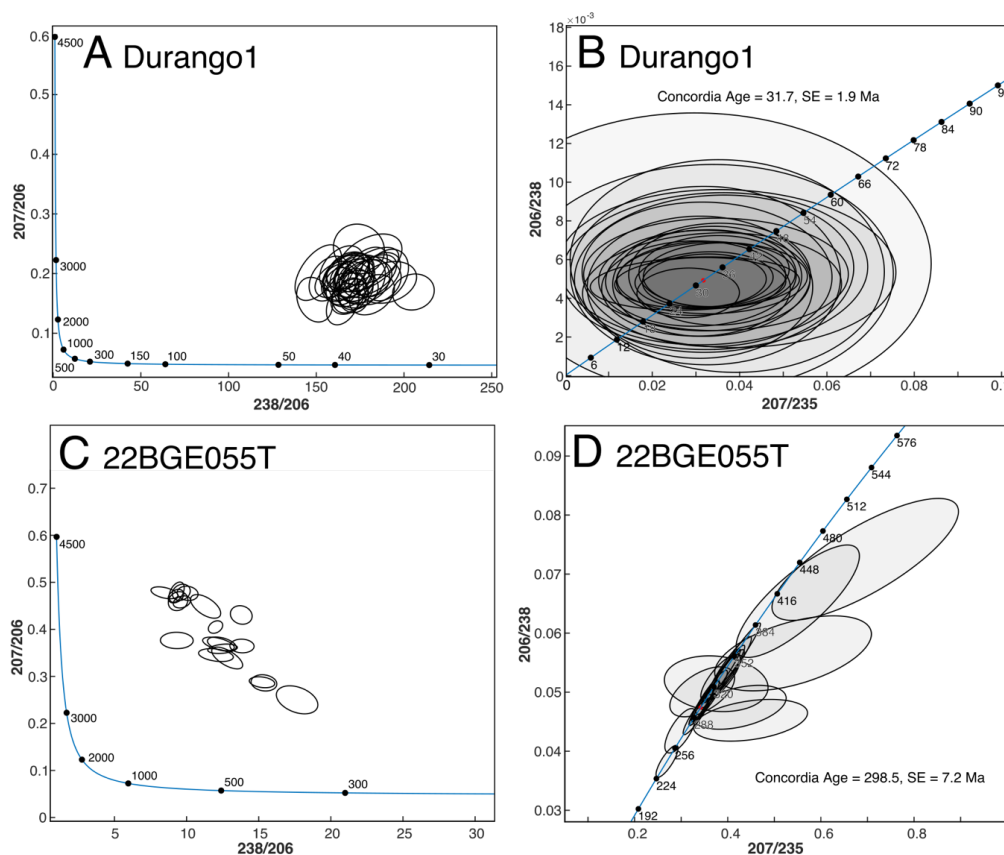
444 4.3 U-Pb Age

445

446 The U-Pb analyses of Durango1 apatite exhibit a narrow range in common Pb composition, as evidenced by the limited
 447 spread of data points in the Tera-Wasserburg diagram (Fig. 4A). This restricted variation indicates a uniform common-
 448 Pb component across the analysed shards and prevents the construction of a well-constrained discordia line and derive
 449 a meaningful lower intercept age. However, following a ²⁰⁷Pb-based common-Pb correction, all Durango analyses
 450 yield a common Concordia age of 31.7 ± 1.9 Ma (Fig. 4B). Additionally, the concordant U-Pb data (defined here as
 451 80-120% concordance) yield an average ²⁰⁸Pb/²³²Th age of 33.0 ± 3.1 Ma which agrees well with the independently



452 constrained crystallization age of 31.44 ± 0.18 Ma from stratigraphically bracketing ignimbrites (McDowell et al.
453 2005). U-Pb data of sample Durango1 were derived with a laser pit diameter of $30 \mu\text{m}$, while a $24 \mu\text{m}$ laser pit diameter
454 was used for Durango2, resulting in significantly higher uncertainties. For instance, concordant $^{208}\text{Pb}/^{232}\text{Th}$
455 measurements yield an average age of 34.0 Ma with a standard deviation of 6.2 Ma, which is twice the standard
456 deviation obtained for comparable measurements with a laser pit diameter of $30 \mu\text{m}$ (Durango1).
457 In contrast, apatite grains from sample 22BGE055T contain a more significant and variable component of common
458 Pb, resulting in considerable scatter in the Tera-Wasserburg diagram and preventing direct age determination through
459 regression (Fig. 4C). After common-Pb correction, the subset of analyses with concordant U-Pb ratios yields an
460 average $^{206}\text{Pb}/^{238}\text{U}$ age of 290.1 ± 25.0 Ma, while the weighted concordia age is 298.5 ± 7.2 Ma (Fig. 4D). These U-
461 Pb ages are slightly younger than previously reported K-Ar biotite and hornblende cooling ages of $320\text{--}330$
462 Ma (Kreuzer and Harre 1975). The typical closure of the U-Pb system in apatite has been determined at $350\text{--}570^\circ\text{C}$
463 (Cherniak et al. 2010), and is therefore somewhat higher than that of the K-Ar biotite system modelled at $280\text{--}345^\circ\text{C}$
464 for cooling rates of $1\text{--}100^\circ\text{C}/\text{Myr}$ (Harrison et al. 1985). Potential reasons for ‘too’ young apatite U-Pb compared to
465 K-Ar ages are (i) regional variations in ages or (ii) sample specific variations in closure temperatures. For instance,
466 diffusion of Pb from U-rich to U-low can significantly increase whole-grain and in-situ apatite U-Pb (e.g., Paul et al.,
467 2019). Regardless, available ages are similar, suggesting rapid post-emplacement cooling, consistent with other
468 basement highs in Central Europe, such as the Black Forest (Timar-Geng et al. 2006) and the Thuringian Forest
469 (Thomson and Zeh 2000).
470



471

472 Figure 4: Apatite U-Pb data for Durango1 and 22BGE055T. A,C) Tera-Wasserburg diagram. B,D) Concordia

473 diagram with derived concordia age and standard error (SE).

474

475

476 4.4 Fission Track Age

477

478 Fission track analyses were conducted on apatite samples Durango2 and 22BGE055T, with only a subset of selected
 479 grains successfully dated due to the method's strict requirements for c-axis parallel orientation and undisturbed internal
 480 grain surfaces (Table 3). The Durango2 apatite, characterized by a low uranium concentration averaging 13.1 ± 1.3
 481 ppm and a relatively small counting area ($30 \mu\text{m}$ diameter), yielded a low number of counted tracks (4 ± 2 on average
 482 per counted area). Consequently, individual ages show wide variation, ranging from 0.0 ± 10.3 Ma to 61.0 ± 21.6 Ma.
 483 The resulting central age of 35.0 ± 4.4 Ma overlaps with the independently determined $^{40}\text{Ar}/^{39}\text{Ar}$ age of 31.44 ± 0.18
 484 Ma for Durango apatite (McDowell et al., 2005).

485 In contrast, sample 22BGE055T displays significantly higher uranium concentrations (59.7 ± 24.5 ppm), which, along
 486 with older apparent ages, led to 17 ± 6 tracks counted in average on the $30 \mu\text{m}$ laser footprint. Single spot/grain ages



487 for this sample range from 37.8±13.4 Ma to 129.3±31.6 Ma, with a central age of 92.1±5.8 Ma, well within the
 488 established AFT age range for the Odenwald region (~70–105 Ma; Wagner, 1969). Additionally, 68 confined track
 489 lengths were measured for 22BGE055T, yielding relatively short tracks with a mean track length (MTL) of
 490 12.61±1.20 μm (Fig. 7C), indicative of substantial annealing.

491

492 Table 3: Apatite fission track results of Durango2 and 22BGE055T.

Sample	Pit diameter (μm)	Laser fluence (J/cm2)	Ablation time (sec)	Ns	Nd (tracks/cm2)	U (ppm)	U1σ (ppm)	Dpar (μm)	Age (Ma)	Age 1σ (Ma)
Durango2										
Grain01	24	3	30	3	1.53E+05	12.28	0.06	1.54	30.2	17.4
Grain02	24	3	30	3	1.53E+05	13.71	0.05	1.71	27.0	15.6
Grain03	24	3	30	1	5.09E+04	13.68	0.05	1.70	9.0	9.0
Grain04	24	3	30	5	2.04E+05	15.13	0.06	1.65	40.8	18.3
Grain05	24	3	30	7	3.06E+05	13.82	0.05	1.62	62.4	23.6
Grain06	24	3	30	not c-axis parallel		11.82	0.05	-	-	-
Grain07	24	3	30	4	1.53E+05	11.94	0.05	1.59	41.3	20.7
Grain08	24	3	30	5	1.53E+05	11.68	0.05	1.59	52.7	23.6
Grain09	24	3	30	2	5.09E+04	12.16	0.05	1.61	20.3	14.4
Grain10	24	3	30	2	1.02E+05	12.08	0.05	1.88	20.4	14.5
Grain11	24	3	30	0	0.00E+00	12.03	0.05	1.62	0.0	10.3
Grain12	24	3	30	6	2.55E+05	11.86	0.05	1.56	62.3	25.5
Grain13	24	3	30	dislocations		15.23	0.06	-	-	-
Grain14	24	3	30	dislocations		15.22	0.06	-	-	-
Grain15	24	3	30	not c-axis parallel		13.42	0.06	-	-	-
Grain16	24	3	30	4	2.04E+05	13.24	0.05	1.62	37.3	18.7
Grain17	24	3	30	4	1.53E+05	13.29	0.05	1.48	37.1	18.6
Grain18	24	3	30	3	1.53E+05	12.51	0.05	1.63	29.6	17.1
Grain19	24	3	30	dislocations		16.49	0.06	-	-	-
Grain20	24	3	30	dislocations		16.17	0.06	-	-	-
Grain21	24	3	30	3	1.02E+05	11.92	0.05	1.51	31.1	18.0
Grain22	24	3	30	dislocations		16.02	0.06	-	-	-
Grain23	24	3	30	8	4.07E+05	16.15	0.07	1.40	61.0	21.6
Grain24	24	3	30	3	1.53E+05	13.90	0.04	1.67	26.6	15.4
Grain25	24	3	30	4	1.53E+05	14.88	0.06	1.60	33.2	16.6
Average				4±2	1.61±0.95E05	13.1±1.3		1.61±0.10	35.0±4.4	
22BGE055T										
Grain01	24	3	30	17	1.71E+06	31.8	0.1	1.64	129.3	31.6
Grain02	24	3	30	not c-axis parallel		42.0	0.2	-	-	-
Grain03	24	3	30	18	1.70E+06	-	-	1.63	-	-
Grain04	24	3	30	not c-axis parallel		83.9	0.4	-	-	-
Grain05	24	3	30	14	2.17E+06	52.8	0.3	1.49	98.9	26.6
Grain06	24	3	30	21	1.87E+06	35.5	0.2	1.74	127.0	27.9
Grain07	24	3	30	9	1.57E+06	47.2	0.2	1.56	80.4	26.9
Grain08	24	3	30	24	3.86E+06	96.3	0.5	1.64	96.7	19.9
Grain09	24	3	30	18	1.98E+06	47.8	0.2	1.65	99.6	23.6
Grain10	24	3	30	19	2.79E+06	58.6	0.3	1.54	114.7	26.5
Grain11	24	3	30	9	1.47E+06	32.7	0.2	1.60	107.9	36.1
Grain12	24	3	30	8	1.56E+06	100.3	0.6	1.62	37.8	13.4
Grain13	24	3	30	21	1.62E+06	53.6	0.3	1.53	72.8	16.0
Grain14	24	3	30	6	7.38E+05	30.3	0.2	1.36	58.9	24.1
Grain15	24	3	30	17	1.53E+06	35.8	0.2	1.56	103.0	25.2
Grain17	24	3	30	18	2.01E+06	61.2	0.3	1.56	79.2	18.8
Grain18	24	3	30	15	2.22E+06	66.1	0.4	1.54	81.0	21.0
Grain19	24	3	30	25	4.86E+06	111.2	0.6	1.72	105.1	21.2
Grain20	24	3	30	10	2.13E+06	62.7	0.4	1.60	81.9	26.0
Grain21	24	3	30	26	3.25E+06	83.6	0.5	1.53	93.6	18.5
Grain22	24	3	30	27	2.97E+06	67.7	0.4	1.68	105.7	20.5
Average				17±6	2.21±0.97E06	59.7±24.5		1.59±0.09	92.1±5.8	

493

494

495

496 4.5 (U-Th)/He Age



497

498 In-situ (U-Th)/He age measurements were conducted on three samples: Durango1, Durango2, and 22BGE055T,
499 yielding consistent results that validate the analytical approach and highlight the influence of grain-specific factors on
500 age variability.

501 Measured He concentrations for Durango1 ranged from 0.0034 to 0.0277 ncc, approximately 0.75 to 6 times the blank
502 level, resulting in standard deviations between 8.6% and 1.1%, respectively (Table 4). The calculated He
503 concentrations varied from 5.39 to 7.63×10^{-20} mol/ μm^3 , with corresponding Sm, Th, and U concentrations spanning
504 232–320 ppm, 357–497 ppm, and 16–26 ppm, respectively. The resulting single-spot in-situ ages for Durango1 ranged
505 from 28.9 to 34.7 Ma, with an average age of 31.04 ± 1.04 Ma ($n = 35$).

506 Durango2 yielded measured He concentrations between 0.0111 and 0.0199 ncc, equating to approximately 15 to 28
507 times the blank level, with low standard deviations of 2.8% to 1.1% (Table 4). He concentrations for Durango2 varied
508 from 3.83 to 6.80×10^{-20} mol/ μm^3 , while Sm, Th, and U concentrations were 139–353 ppm, 250–442 ppm, and 11–
509 16 ppm, respectively. Single-grain ages from 22 spot analyses ranged from 23.8 to 34.5 Ma, with an average age of
510 31.38 ± 2.53 Ma. Notably, the derived in-situ ages for Durango1 and Durango2 are in excellent agreement with the
511 independently determined $^{40}\text{Ar}/^{39}\text{Ar}$ age of 31.44 ± 0.18 Ma and the whole-grain apatite age of 31.02 ± 1.01 Ma
512 (McDowell et al., 2005).

513 For sample 22BGE055T, the measured He content of individual laser-ablation pits ranged from 0.0033 to 0.0167 ncc,
514 corresponding to 4 to 20 times the line blank level, with standard deviations of 1.6% to 5.7% (Table 4). Laser pits
515 with diameters of 30 μm yielded pit volumes of 3237 to 3987 μm^3 , resulting in He concentrations of 0.41 to 1.87×10^{-19}
516 mol/ μm^3 . Associated Sm, Th, and U concentrations varied widely from 15–296 ppm, 11–149 ppm, and 30–123 ppm,
517 respectively. The resulting in-situ (U-Th)/He ages for 22BGE055T displayed significant variation, ranging from
518 36.2 ± 10.0 to 106.8 ± 2.5 Ma. This large range is attributed to factors such as grain size (e.g., Grain07), ambiguous
519 grain geometry (e.g., Grain04), and pronounced element zoning (e.g., Grain12 and Grain21). Excluding grains with
520 these complexities yields a mean age of 71.5 ± 21.5 Ma, compared to 73.0 ± 19.0 Ma when all grains are included. The
521 greater dispersion in ages relative to the Durango standards is expected, given the variations in grain size, radionuclide
522 concentrations, and the more complex thermal history of sample 22BGE055T.

523

524 Table 4: In-situ apatite (U-Th)/He results of Durango1, Durango2 and 22BGE055T.



Sample	Pit diameter (µm)	Laser fluence (J/cm ²)	Ablation time (sec)	4He (ncc)	4He 1σ (%)	4He (mol)	4He 1σ (mol)	Pit volume (µm ³)	Pit volume 1σ (µm ³)	4He (mol/µm ³)	4He 1σ (mol/µm ³)	Sm (ppm)	Sm 1σ (ppm)	Th (ppm)	Th 1σ (ppm)	U (ppm)	U 1σ (ppm)	eU (ppm)	Age (Ma)	Age 1σ (Ma)	Laser pit	Element zoning	Grain geometry	Pit-Grain relation
Durango1	50	1.3	4	0.0068	5.8	3.03E-16	1.77E-17	5123	3	5.91E-20	1.43E-21	306.4	10.9	375.0	8.3	19.1	0.4	107.3	31.6	1.0	0	0	na	0
Grain01	50	1.3	4	0.0039	3.8	1.75E-16	6.59E-18	2628	43	6.64E-20	1.69E-21	306.3	10.7	384.4	8.4	19.4	0.4	109.7	34.7	1.1	0	0	na	0
Grain03	50	1.3	6	0.0096	3.2	4.26E-16	1.35E-17	7222	4	5.90E-20	1.05E-21	305.9	10.8	392.8	8.6	19.1	0.4	111.4	30.4	0.8	0	0	na	0
Grain04	50	1.3	2	0.0034	8.3	5.52E-16	1.26E-17	2738	6	5.54E-20	1.60E-21	247.9	8.9	368.3	8.1	17.8	0.4	104.3	30.5	1.0	0	0	na	0
Grain05	50	1.3	4	0.0066	6.0	2.94E-16	1.75E-17	5281	2	5.57E-20	1.36E-21	250.9	9.0	371.4	8.2	17.8	0.4	105.1	30.4	1.0	0	0	na	0
Grain06	50	1.3	6	0.0092	2.7	4.10E-16	1.11E-17	7381	11	5.55E-20	9.20E-22	239.1	8.6	364.6	8.0	17.4	0.4	103.1	30.9	0.8	0	0	na	0
Grain07	50	1.5	8	0.0137	2.5	6.11E-16	1.53E-17	11253	20	5.43E-20	8.65E-22	243.3	8.8	368.0	8.1	17.3	0.4	103.8	30.0	0.7	0	0	na	0
Grain08	50	2.0	8	0.0169	2.2	7.55E-16	1.63E-17	13695	23	5.51E-20	8.16E-22	244.2	8.9	359.0	8.0	17.2	0.4	101.5	31.2	0.7	0	0	na	0
Grain09	50	2.5	8	0.0207	1.7	9.22E-16	1.52E-17	16051	7	5.75E-20	7.99E-22	297.0	10.7	378.6	8.4	18.5	0.4	107.5	30.7	0.7	0	0	na	0
Grain10	50	3.0	8	0.0234	1.8	1.05E-15	1.88E-17	18351	12	5.69E-20	7.65E-22	292.3	10.6	388.0	8.6	18.7	0.4	109.9	29.7	0.7	0	0	na	0
Grain11	50	1.3	6	0.0139	3.3	6.19E-16	2.05E-17	11486	4	5.99E-20	9.81E-22	302.2	10.9	377.6	8.4	18.3	0.4	107.0	28.9	0.8	0	0	na	0
Grain12	50	1.3	6	0.0087	4.4	3.90E-16	1.73E-17	6788	4	5.74E-20	1.21E-21	269.5	9.8	376.9	8.3	17.1	0.4	105.7	31.2	0.9	0	0	na	0
Grain16	50	1.3	2	0.0034	8.6	5.52E-16	1.11E-17	2450	1	6.20E-20	1.62E-21	278.9	10.3	387.2	8.6	20.6	0.5	111.6	31.9	1.1	0	0	na	0
Grain17	50	1.3	2	0.0034	7.8	1.50E-16	1.18E-17	2699	6	5.55E-20	1.64E-21	290.3	10.8	362.8	8.2	19.9	0.5	105.2	30.3	1.0	0	0	na	0
Grain18	50	1.3	4	0.0076	3.6	3.41E-16	1.24E-17	5493	72	6.21E-20	1.44E-21	273.6	10.4	384.2	8.7	21.0	0.5	111.3	32.0	0.9	0	0	na	0
Grain19	50	1.3	4	0.0074	4.5	3.31E-16	1.48E-17	5111	104	6.35E-20	1.85E-21	298.3	11.0	399.5	8.8	20.4	0.5	112.8	34.3	1.1	0	0	na	0
Grain20	50	1.3	8	0.0120	3.4	5.35E-16	1.82E-17	8900	41	5.46E-20	1.03E-21	279.8	10.4	357.1	8.0	18.9	0.4	102.9	30.5	0.8	0	0	na	0
Grain21	50	1.3	3	0.0132	3.3	5.90E-16	1.94E-17	10502	31	5.62E-20	1.03E-21	289.1	10.6	381.8	8.5	18.3	0.4	108.1	29.9	0.8	0	0	na	0
Grain22	50	1.3	8	0.0130	2.3	5.80E-16	1.32E-17	10509	10	5.52E-20	8.34E-22	287.1	10.5	376.8	8.4	18.2	0.4	106.7	29.7	0.7	0	0	na	0
Grain23	50	1.3	8	0.0134	2.8	5.54E-16	1.49E-17	8960	11	5.71E-20	9.31E-22	258.7	9.5	378.3	8.1	16.1	0.4	105.2	31.2	0.8	0	0	na	0
Grain24	50	1.3	8	0.0125	3.1	5.60E-16	1.75E-17	9400	23	5.95E-20	1.06E-21	257.4	9.3	385.2	8.5	16.2	0.4	106.7	32.0	0.8	0	0	na	0
Grain25	50	1.5	8	0.0145	2.8	6.49E-16	1.82E-17	11111	22	5.84E-20	9.95E-22	298.1	10.6	391.0	8.6	18.6	0.4	110.5	30.3	0.8	0	0	na	0
Grain26	50	1.5	8	0.0154	1.4	6.33E-16	1.31E-17	10826	89	5.78E-20	1.18E-21	281.8	10.3	387.6	8.2	17.8	0.4	109.0	31.7	0.9	0	0	na	0
Grain27	50	1.5	8	0.0155	1.6	6.93E-16	1.08E-17	10633	76	6.52E-20	9.38E-22	254.3	10.1	428.3	10.8	17.1	0.4	117.7	31.8	0.9	0	0	na	0
Grain28	50	2.0	8	0.0190	2.0	8.47E-16	1.70E-17	14243	165	5.95E-20	1.09E-21	241.9	9.5	405.1	10.1	16.4	0.4	111.5	30.7	0.8	0	0	na	0
Grain29	50	2.0	8	0.0176	1.9	8.87E-16	1.48E-17	13803	15	5.70E-20	7.83E-22	224.5	10.2	369.8	8.1	15.4	0.4	109.8	30.9	0.8	0	0	na	0
Grain30	50	2.5	8	0.0206	1.5	9.21E-16	1.38E-17	16123	27	5.71E-20	7.07E-22	240.5	8.7	383.5	8.5	17.8	0.4	108.0	30.4	0.7	0	0	na	0
Grain31	50	2.5	8	0.0217	1.8	9.67E-16	1.77E-17	15995	68	6.05E-20	8.57E-22	292.4	10.4	398.5	8.8	20.1	0.4	113.7	30.5	0.7	0	0	na	0
Grain32	50	2.0	8	0.0172	1.1	1.24E-15	1.37E-17	18197	13	7.43E-20	8.07E-22	278.8	11.3	497.7	11.0	25.9	0.6	142.8	30.8	0.7	0	0	na	0
Grain33	50	2.0	8	0.0188	2.7	8.41E-16	2.26E-17	13666	55	6.15E-20	1.04E-21	282.2	10.0	391.3	8.6	20.5	0.5	112.5	31.4	0.8	0	0	na	0
Grain35	50	3.0	8	0.0255	1.6	1.14E-15	1.85E-17	18148	20	6.28E-20	8.04E-22	299.7	11.1	383.5	9.2	20.4	0.5	110.5	32.6	0.8	0	0	na	0
Grain36	50	3.0	8	0.0237	1.6	1.06E-15	1.67E-17	18514	57	5.73E-20	7.85E-22	261.8	9.3	376.3	8.2	16.6	0.4	105.1	31.2	0.7	0	0	na	0
Average										5.91E-20	4.4E-22	278.25		385.24		18.721.9		109.7		31.041.04				
Durango2	30	2.0	8	0.0088	3.0	3.94E-16	7.68E-18	2123	-	3.03E-20	5.93E-22	363.9	55.2	367.8	2.1	12.42	0.17	98.9	17.5	0.4	5	0	na	0
Grain02	30	2.0	8	0.0153	2.3	6.83E-16	1.54E-17	7359	-	2.52E-20	1.18E-21	353.5	54.4	315.8	2.9	13.09	0.10	87.3	34.5	0.8	0	0	na	0
Grain03	30	2.0	8	0.0152	2.1	6.78E-16	1.42E-17	9057	-	5.22E-20	1.09E-21	251.5	39.3	326.8	3.1	13.49	0.10	90.3	33.1	0.8	0	0	na	0
Grain04	30	2.0	8	0.0182	1.5	6.12E-16	1.18E-17	7065	-	6.25E-20	9.16E-22	271.8	42.8	381.3	3.7	15.04	0.12	104.6	34.3	0.6	0	0	na	0
Grain05	30	2.0	8	0.0054	3.0	2.39E-16	7.18E-18	2109	-	1.84E-20	5.52E-22	202.4	32.1	322.6	3.2	13.89	0.11	89.7	11.8	0.4	5	0	na	0
Grain06	30	2.0	8	0.0119	1.7	3.31E-16	9.29E-18	5577	-	4.09E-20	1.75E-22	260.4	41.7	265.6	2.8	10.81	0.09	73.2	32.0	0.6	0	0	na	0
Grain07	30	2.0	8	0.0128	2.2	5.73E-16	1.28E-17	7819	-	4.41E-20	9.85E-22	224.5	36.2	298.7	3.9	11.73	0.11	81.9	30.9	0.8	0	0	na	0
Grain08	30	2.0	8	0.0111	2.5	4.97E-16	1.22E-17	6531	-	3.83E-20	9.40E-22	192.1	31.2	270.3	2.9	11.06	0.09	74.6	29.4	0.8	0	0	na	0
Grain09	30	2.0	8	0.0124	2.8	5.55E-16	1.53E-17	6400	-	4.27E-20	1.18E-21	245.4	40.6	266.5	2.7	11.22	0.10	73.9	33.1	1.0	0	0	na	0
Grain10	30	2.0	8	0.0125	2.0	5.58E-16	1.11E-17	7398	-	4.29E-20	8.51E-22	277.2	46.2	365.8	2.7	11.35	0.10	73.8	33.3	0.7	0	0	na	0
Grain11	30	2.0	8	0.0125	1.9	5.60E-16	1.07E-17	7592	-	4.31E-20	8.26E-22	270.2	45.4	267.5	2.8	11.26	0.10	74.1	33.3	0.7	0	0	na	0
Grain12	30	2.0	8	0.0115	2.5	5.14E-16	1.29E-17	7427	-	3.95E-20	9.94E-22	277.9	47.1	249.8	2.6	11.75	0.11	70.4	32.1	0.8	0	0	na	0
Grain13	30	2.0	8	0.0137	1.7	6.14E-16	1.07E-17	7204	-	4.72E-20	8.21E-22	216.1	37.0	337.7	3.5	14.87	0.14	94.2	28.8	0.5	0	0	na	0
Grain14	30	2.0	8	0.0128	2.0	5.70E-16	1.11E-17	7905	-	4.39E-20														



538

539

540 **5.1 He diffusion and fission track annealing during mounting**

541

542 Each dating method applied in this study (fission track (FT), in situ (U-Th)/He, and U-Pb) requires specific sample
543 preparation constraints to ensure analytical precision and reliability. For instance, fission tracks must be etched to
544 become optically visible, necessitating chemically resistant embedding media. Traditionally, epoxy is used for apatite
545 FT and U-Pb analysis, whereas thin Teflon films are preferred for zircon due to their resistance to etchants and optical
546 transparency. In contrast, in situ (U-Th)/He dating requires sample mounts that are ultra-high vacuum (UHV)
547 compatible, which excludes most conventional epoxies due to their relatively high vapor pressure. Additionally, for
548 laser ablation inductively coupled plasma mass spectrometry (LA-ICP-MS) analyses used in U-Pb dating and trace
549 element measurements, a rigid and flat mount surface is essential. This ensures consistent laser focus and reproducible
550 ablation pit geometry, which are critical for accurate dating and elemental quantification. As a result, epoxy mounts
551 are commonly used in these applications.

552 Implementing double or triple dating on the same grains requires a methodological compromise, given the differing
553 mounting requirements of each technique. Previous studies have proposed various solutions, such as re-mounting
554 grains from epoxy into indium (e.g., Boyce et al., 2016), using Teflon-aluminium composite mounts (Pickering et al.,
555 2020), or embedding directly in Teflon (e.g., Tripathy-Lang et al., 2013; Evans et al., 2015). However, each method
556 has limitations. Re-mounting is labour-intensive and carries the risk of grain loss, while Teflon-aluminium composites
557 are opaque, making them unsuitable for transmitted light microscopy necessary for FT counting.

558 The embedding method applied here using Teflon film requires heating grains to temperatures close to 300°C, clearly
559 exceeding the temperature at which He diffusion and fission track annealing in apatite is significant over geological
560 timescales (e.g. Ketcham et al. 1999; Farley 2000). We therefore evaluated the effect of the mounting using 1D thermal
561 history modelling and comparing fission track length distributions of samples mounted with epoxy (without heating)
562 and Teflon (with heating). The modelling indicates that brief heating (~1.5 minutes at 300 °C) does not affect apatite
563 (U-Th)/He or fission track ages, and results in only minimal track length reduction. For previously unannealed
564 fluorapatite grains, the model predicts a reduction of ~0.1 µm, which would be even smaller for more annealing-
565 resistant tracks (e.g., pre-annealed or Cl-rich apatite). Consistent with this, measured mean track lengths (MTL) from
566 fluorapatites in southwestern Germany with pre-annealed tracks show only a minor reduction of 0.03 µm (13.12 µm
567 in epoxy vs. 13.09 µm in Teflon mounts). Thus, embedding apatites in Teflon at 300 °C does not lead to significant
568 He diffusion or FT annealing. However, careful control of heating duration and temperature during mounting is
569 essential.

570

571

572

573 **5.2 Excluding individual spot analysis when applying the in-situ (U-Th)/He method**

574



575 As detailed in Sect. 2, the in-situ (U-Th)/He dating protocol involves a series of preparation and analytical steps that
576 can be lengthy and technically demanding. Consequently, not all grains subjected to this procedure will yield data
577 suitable for interpretation. To maintain data quality and analytical consistency, it is essential to apply pre-defined
578 exclusion criteria for the selection of acceptable grains. Based on our experience and previous studies, we propose a
579 decision matrix that evaluates four key criteria: laser pit shape, radionuclide zoning, grain geometry, and the pit–grain
580 relationship (Fig. 5).

581

582 *Laser pit shape*

583 The laser pit shape is influenced both by the laser beam properties and the physical condition of the grain surface.
584 Ideally, the laser pit should be circular with steep, vertical walls and a flat base, characteristics that occur when the
585 laser energy is evenly distributed, the focus is precise, and the grain surface is free of roughness, inclusions, or fractures
586 (Fig. 5). Deviations from these ideal conditions, such as irregular pit outlines, sloping walls, or surface chipping,
587 complicate accurate volume estimation and may lead to incomplete helium release during ablation. Pits that display
588 significant edge overlap or evidence of chipped-off fragments should be excluded from interpretation.

589

590 *Radionuclide zoning*

591 In terms of radionuclide zoning, it is important to recognize that the measured helium originates from a surrounding
592 diffusion domain approximately 40 μm in radius. However, due to the partial removal of this domain during grinding
593 and polishing, only a fraction of the total helium-producing volume is retained in the final measurement. Consequently,
594 even visually homogeneous grains may still be influenced by zoning within the original contributing volume. To
595 evaluate the uniformity of the radionuclide distribution in the ablation zone, we propose the use of the mean square of
596 weighted deviates (MSWD) determined for the depth-corrected radionuclide concentrations as a diagnostic metric. A
597 value near 1 suggests a uniform distribution of parent nuclides, while elevated MSWD values indicate significant
598 zoning or compositional heterogeneity. Grains with pronounced zoning, visible inclusions, or MSWD values
599 exceeding 20 should be excluded to ensure reliable interpretation.

600

601 *Grain geometry*

602 The geometry of the mineral grain is another critical factor affecting the accuracy of in-situ (U-Th)/He analyses. Since
603 alpha particles have long alpha stopping distances (up to 40 μm), grain shape influences both helium production and
604 retention. Ideally, analyses should target euhedral grains with well-preserved, flat prismatic surfaces. Complex or
605 irregular morphologies introduce uncertainties in modeling alpha-ejection and diffusion pathways.

606 Precise characterization of the grain, particularly its dimensions and the location of the laser pit, is essential for thermal
607 history modelling. Of primary importance is the distance from the laser pit to the nearest prismatic face and to the
608 grain tip. These distances must be well constrained and visually verifiable. In cases where the tips of long-prismatic
609 crystals are broken, reliable modelling remains feasible if the preserved prism length is at least twice the grain
610 diameter. Subhedral grains generally should be excluded due to their ambiguous geometry; however, exceptions can



611 be made for large shards (e.g., Durango apatite), where geometric uncertainties have a negligible impact on resulting
612 ages.

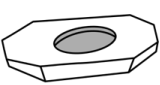
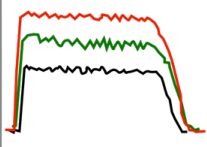
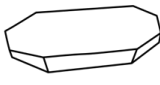
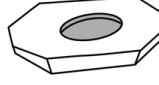
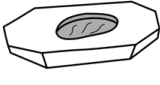
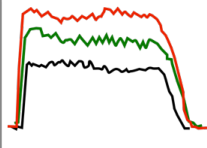

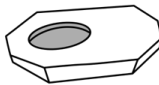

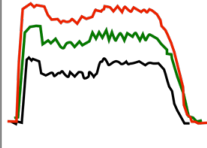

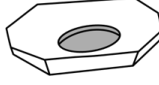
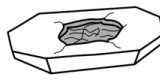
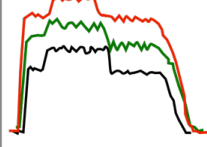

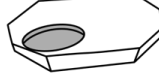

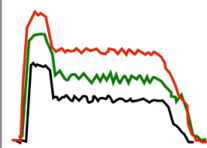

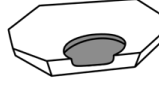
613

614 *Pit-grain relationship*

615 The spatial relationship between the laser-ablation pit and the mineral grain must be carefully considered due to the
616 relatively long alpha-stopping distances. Ideally, the pit should be located near the center of the grain to minimize
617 edge effects and ensure a well-constrained alpha-ejection correction. Slight deviations toward the prismatic face or
618 grain tip are acceptable, provided the pit remains fully within the grain and avoids complex or irregular edges.

619 Measurements where the pit is too close to highly curved or irregular boundaries introduce geometric uncertainties
620 and should be treated with caution. In particular, pits that are partly outside the grain must be excluded, as they
621 compromise both the helium yield and the alpha-ejection correction, leading to unreliable age estimates.



	Laser pit shape	Radio-nuclide zoning	Grain geometry	Pit-grain relationship
1 - perfect	 round, vertical walls, flat bottom	 uniform, MSWD ~1	 euhedral grain with minimal surface curvature	 pit centered, far from edges
2	 slightly irregular shape or depth	 slight variations, MSWD >1	 slightly deformed euhedral grain	 pit not centered, but >40 μm away from edges
3	 rough surfaces or broken edges	 moderate zoning, MSWD >5	 partly broken euhedral grain	 pit not centered, and <40 μm away from edges
4	 strong surface roughness	 strong zoning, MSWD >10	 euhedral grain with tips broken off, subhedral grain	 pit not centered, and <40 μm away from edges
5 - excluded	 chipped off or incomplete	 extreme zoning, MSWD >20	 subhedral grain, without clear grain boundaries	 pit crosses grain edge



623 Figure 5: Decision matrix to rank/exclude in-situ (U-Th)/He measurements. The red, green and black lines in the
 624 second column (Radionuclide zoning) represent counts measured by LA-ICP-MS for trace elements such as
 625 radionuclides (U, Th, Sm).

626

627

628 5.3 Thermal history reconstruction

629

630 To reconstruct the thermal evolution of the crystalline basement in the Odenwald region, we performed inverse thermal
 631 history modelling of sample 22BGE055T. This sample was collected from exposed granodioritic basement and
 632 represents a key location for understanding the post-Variscan to Cenozoic cooling and exhumation history of the
 633 Odenwald. The modelling approach combines apatite fission track (AFT) data and in-situ (U-Th)/He
 634 thermochronometry, utilizing the annealing model of Ketcham et al. (2007) for fission tracks and the diffusion model
 635 of Flowers et al. (2009), adapted for in-situ measurements following Glotzbach and Ehlers (2024).

636 The input dataset includes a central AFT age of 92.1 ± 5.8 Ma, a measured track length distribution with a mean track
 637 length (MTL) of 12.61 ± 1.20 μm , a Dpar of 1.59 μm , and a set of 15 single-grain in-situ He measurements, each
 638 accompanied by detailed radionuclide concentrations and grain-specific geometries (see Table 5). To avoid unrealistic
 639 thermal histories, we applied three independent geological time-temperature (tT) constraints. The first is based on the
 640 concordant apatite U-Pb age of 298.5 ± 7.2 Ma (Fig. 4D), corresponding to temperatures between 370 and 500°C
 641 (Mezger et al., 1989), indicative of late-stage cooling after pluton emplacement. The second constraint corresponds to
 642 Early Triassic time (247.5 – 252.5 Ma), when Buntsandstein deposition occurred across the region. At that time, the
 643 sampled crystalline basement was several hundred meters below the surface, and the temperature was therefore
 644 constrained to 20 – 50°C . The third constraint is the present-day surface temperature, fixed at 10°C .

645

646 Table 5: In-situ apatite (U-Th)/He data input for thermal history modelling of sample 22BGE055T.

Sample	He (at/g)	He 1 σ (at/g)	U (ppm)	U 1 σ (ppm)	Th (ppm)	Th 1 σ (ppm)	Sm (ppm)	Sm 1 σ (ppm)	Dist2PrismX (μm)	Dist2PrismZ (μm)	Grain Radius (μm)	Pit Radius (μm)	Pit Depth (μm)
Grain01	1.24E+16	4.89E+14	33.3	0.2	72.5	0.4	57.6	5.5	91	94	128	15	7
Grain02	9.29E+15	5.31E+14	41.4	0.3	26.0	0.1	79.5	7.7	120	112	131	15	7
Grain05	1.41E+16	4.32E+14	47.9	0.3	25.6	0.1	15.2	1.5	49	57	58	15	7
Grain06	1.22E+16	4.68E+14	34.7	0.2	44.9	0.2	54.3	5.4	76	77	104	15	7
Grain07	1.21E+16	6.31E+14	50.8	0.4	141.2	1.2	0.0	0.0	28	26	32	15	7
Grain08	2.83E+16	6.91E+14	97.2	0.7	149.8	0.8	178.1	18.2	57	75	97	15	7
Grain09	1.38E+16	6.85E+14	47.1	0.3	50.7	0.3	49.1	5.1	35	61	85	15	7
Grain11	1.22E+16	3.86E+14	31.1	0.2	44.1	0.2	30.5	3.2	29	45	38	15	7
Grain13	1.55E+16	4.79E+14	49.6	0.3	97.9	0.5	166.3	18.0	51	53	62	15	7
Grain14	1.05E+16	3.10E+14	29.9	0.2	52.7	0.3	41.2	4.5	50	141	101	15	7
Grain15	1.26E+16	6.52E+14	34.7	0.2	38.1	0.2	24.1	2.7	68	141	101	15	7
Grain17	1.62E+16	3.77E+14	59.4	0.4	14.4	0.1	26.1	2.9	66	55	70	15	7
Grain18	2.23E+16	5.81E+14	66.0	0.5	45.8	0.2	119.9	13.6	53	55	67	15	7
Grain19	3.40E+16	5.45E+14	103.3	0.7	103.9	0.4	295.9	33.8	27	65	67	15	7
Grain20	7.62E+15	4.13E+14	60.5	0.4	12.8	0.1	46.8	5.4	101	62	103	15	7

647

648 Dist2PrismX is the distance of the center of the laser pit towards the closest prism grain edge within the polished
 649 section. Dist2PrismZ is the distance of the polished section towards the grain bottom.

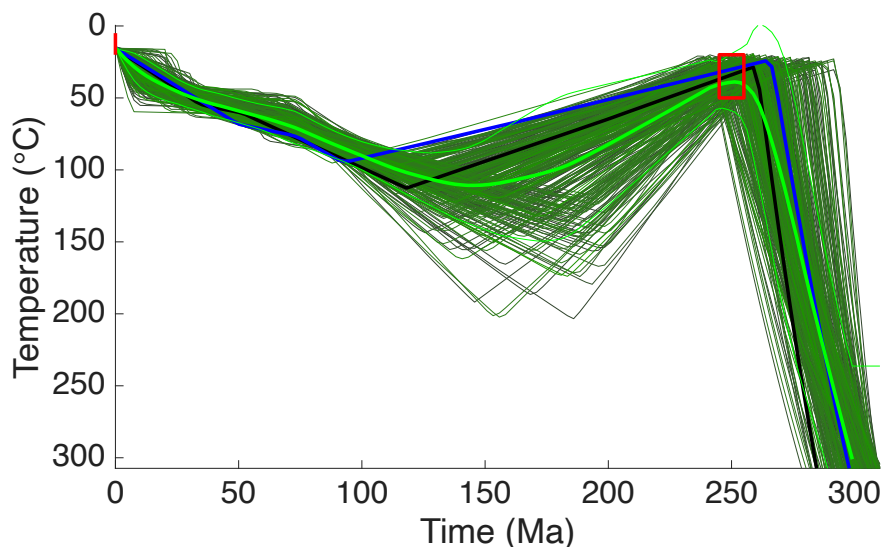
650

651 Given the large and complex dataset, we split the inverse modelling process into two stages to improve computational
 652 efficiency. In the first step, we generated one million random time-temperature paths and evaluated their fit against



653 the fission track age and length distribution. Paths that yielded acceptable goodness-of-fit (GOF) values, as defined
654 by Ketcham (2005), were retained. In the second step, 300 of these acceptable paths were randomly selected and
655 evaluated against the in-situ (U-Th)/He data. Models were ranked according to how many input datasets they could
656 reproduce with a GOF > 0.05 (Fig. 6). Although no single model fit all datasets simultaneously, the best-performing
657 model successfully fit nine datasets: the fission track age, the track length distribution, and seven of the in-situ He
658 concentrations (Fig. 7).

659 The ensemble of successful models reveals a well-defined thermal history, especially after ~150 Ma. Earlier stages
660 are more loosely constrained and rely primarily on the imposed geological tT constraints. Following the emplacement
661 of the granodiorite at ca. 320–330 Ma (Kreuzer and Harre, 1975) and depths of ~15 km (Stein and Dietl, 2001), rapid
662 post-intrusion cooling is supported by the apatite U-Pb age of ~300 Ma. Stratigraphic and thermochronologic evidence
663 suggests that the crystalline basement was largely exhumed by the end of the Permian, followed by a prolonged phase
664 of reheating due to continued sedimentation and burial, likely persisting until the Late Jurassic. The modelled thermal
665 peak exceeded 90°C, sufficient to fully reset both the AFT and AHe systems.



666

667

668 Figure 6: Modelled tT-path of sample 22BGE055T using apatite fission track and in-situ (U-Th)/He data. Paths are
669 color-ranked according to their fit from black to light green with the thick green line is the weighted mean cooling
670 paths with 95% CI (thin green lines). The tT-path that fit best the data is shown in blue (highest summed GOF) and
671 black (most input data fitted with GOF>0.05). The red box is constraining the cooling paths to represent late Permian
672 exhumation to near surface temperatures.

673

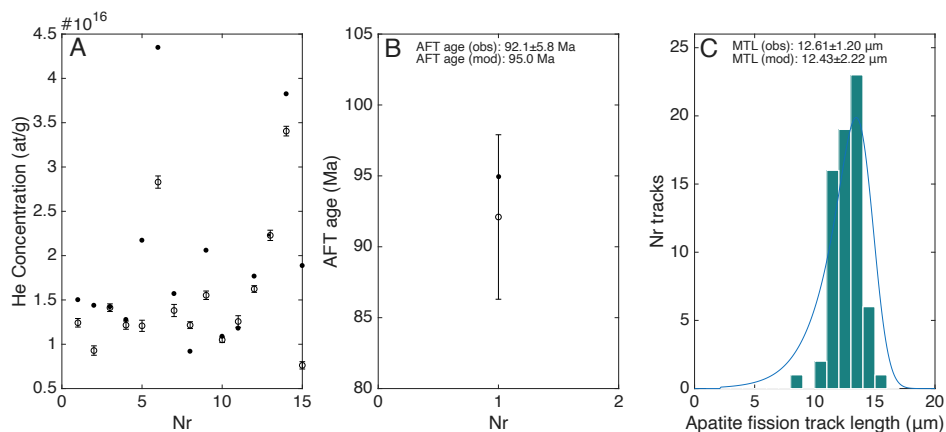
674 The thermochronological data do not precisely resolve the timing of basin inversion, but according to the reconstructed
675 cooling paths it must have occurred before ~90 Ma (Fig. 6). It remains uncertain whether sedimentation ceased at the
676 end of the Jurassic or extended into the Cretaceous. Nevertheless, the modelling identifies two distinct cooling



677 episodes that correlate well with known geodynamic events in the region. The first, during the Late Cretaceous, likely
678 reflects regional doming and erosion, consistent with evidence of contemporaneous volcanism (Binder et al., 2023).
679 For instance, the Messel volcano, located north of the Odenwald, was emplaced on Rotliegend sediments at ~48.2 Ma
680 (Lenz et al. 2014), while the Katzenbuckel volcano, southeast of the Odenwald, intruded Middle Jurassic rocks at ~69
681 Ma (Schmitt et al. 2007). The nearly 1000 meter of difference in erosion level between these sites is largely attributed
682 to regional doming during Late Cretaceous. Nonetheless, the non-synchronous timing of volcanic activity introduces
683 some uncertainty to this estimate. This north-south gradient in pre-Tertiary exhumation is also reflected in the pre-
684 Tertiary geology of the adjacent Upper Rhine Graben (URG) and is attributed to regional uplift and the erosional
685 removal of cover rocks during Late Cretaceous tectonism.

686 The second major cooling phase, occurring after ~40 Ma, aligns with the initial development of the Upper Rhine
687 Graben and the associated uplift of the graben shoulders, including the Odenwald. Since its emplacement, the
688 Katzenbuckel volcano has been eroded down to the Buntsandstein, indicating approximately 600 meters of post-69
689 Ma erosion (e.g. Wagner 1969), consistent with the amount of exhumation required to produce the cooling observed
690 in sample 22BGE055T.

691 In summary, combined thermal history modelling using AFT and apatite in situ (U-Th)/He data can be performed in
692 a manner similar to modelling with AFT and whole-grain (U-Th)/He data. However, when large volumes of in-situ
693 (U-Th)/He data are included, modeling becomes computationally intensive and may significantly slow down. Running
694 the thermal modeling sequentially, as done in this study, rather than simultaneously, offers a practical approach to
695 improve computational efficiency. The inverse thermal modeling of AFT and in-situ (U-Th)/He data for sample
696 22BGE055T reveals a complex thermal evolution, characterized by post-intrusive cooling, burial and reheating during
697 the Mesozoic, and two distinct Cenozoic cooling phases associated with regional tectonic events.



698

699



700 Fig. 7: Observed vs. modelled thermochronological data of sample 22BGE055T and the best fit tT-path that fit most
701 input data simultaneously (black tT-path in Fig. 6).

702

703

704 **6 Conclusion and broader applicability**

705

706 This study introduces a practical and effective analytical method for triple-dating apatite grains using a Teflon-based
707 mounting approach. The method facilitates the integration of AFT, in-situ (U-Th)/He, and U-Pb dating on the same
708 grains, while preserving zoning information and geochemical context. Results presented here from the Durango apatite
709 standard validate the technique's accuracy, and the application to a basement sample from the Odenwald reveals a
710 detailed thermal history in line with major geodynamic episodes of the region. Importantly, we find that neither the
711 fission track system nor helium diffusion are measurably affected during mount preparation. To improve the
712 consistency and reliability of in-situ He data, we propose a decision matrix that aids in evaluating grain suitability
713 based on critical geometric and analytical parameters.

714 This integrated approach presented here opens new possibilities for extracting multi-system geochronological and
715 thermochronological information from single grains, particularly in complex tectonic settings. The relatively rapid
716 sample procedure presented (compared to other protocols) avoids the time-consuming steps of extracting grains and/or
717 remounting them for analysis by different techniques. More rapid sample processing also reduces analytical and labor
718 costs. The procedures presented here enable higher throughput of individual grain analyses per sample. A higher
719 throughput means that detrital samples (e.g., from river sediments, or sedimentary basins) can more easily be
720 characterised for sediment provenance (e.g., Pujols and Stockli, 2021), catchment erosion patterns in locations with
721 heterogeneous bedrock (e.g., Stock et al., 2006; Ehlers et al., 2015; Madella et al., 2022) or hinterland exhumation or
722 basin burial. Characterisation of sediment provenance is also enhanced by measurement of rare earth element
723 variations between grains. Lastly, samples collected from bedrock benefit from this approach via enhanced
724 characterization of inter-grain variability in ages which can lead to more resolute determination of rock cooling
725 histories and geologic interpretations.

726

727 **Code availability**

728 All mentioned scripts and apps together with user manuals describing in detail their usage are available from the
729 associated Zenodo repository (<https://doi.org/10.5281/zenodo.18979745>).

730

731 **Author contributions**

732 Conceptualisation: TAE, CG. Formal analysis: CG, AN. Coding: CG. Visualization: CG. Writing: CG, AN, TAE.

733

734 **Competing interests**

735 The contact author has declared that neither of the authors has any competing interests.

736



737

738

739

740

741 **Financial support**

742 This study was supported by the Bundesgesellschaft für Endlagerung (BGE – STAFuE-21-12-Klei), and funding for
743 large equipment from the Deutsche Forschungsgemeinschaft (DFG) to Todd Ehlers (INST 37/1041-1 FUGG, INST
744 37/1207-1 FUGG).

745

746 **References:**

747 Abdullin, F., Solari, L. A., Solé, J., & Ortega-Obregón, C.: Technical note: LA-ICP-MS U–Pb dating of unetched and
748 etched apatites, *Geochronology*, 3(1), 59–65, <https://doi.org/10.5194/gchron-3-59-2021>, 2021.

749 Bedoya, A., Glorie, S., Hand, M., Kirkland, C. L., Kelsey, D. E., Nixon, A., & Fraser, G.: Apatite Triple Dating (Lu–
750 Hf, U–Pb, FT) Constrains Deformation and Cooling in the Coompana and Madura Provinces, Western Australia,
751 *Lithosphere*, 2023(Special 14), https://doi.org/10.2113/2023/lithosphere_2023_292, 2024.

752 Binder, T., Marks, M. A. W., Gerdes, A., Walter, B. F., Grimmer, J., Beranoaguirre, A., Wenzel, T., Markl, G.: Two
753 distinct age groups of melilitites, foidites, and basanites from the southern Central European Volcanic Province
754 reflect lithospheric heterogeneity, *International Journal of Earth Sciences*, 112(3), 881–905,
755 <https://doi.org/10.1007/s00531-022-02278-y>, 2023.

756 Boyce, J. W., Hodges, K. V., Olszewski, W. J., Jercinovic, M. J., Carpenter, B. D., & Reiners, P. W.: Laser microprobe
757 (U–Th)/He geochronology, *Geochimica et Cosmochimica Acta*, 70(12), 3031–3039,
758 <https://doi.org/10.1016/j.gca.2006.03.019>, 2006.

759 Carrapa, B., DeCelles, P. G., Reiners, P. W., Gehrels, G. E., & Sudo, M.: Apatite triple dating and white mica
760 $^{40}\text{Ar}/^{39}\text{Ar}$ thermochronology of syntectonic detritus in the Central Andes: A multiphase tectonothermal history,
761 *Geology*, 37(5), 407–410, <https://doi.org/10.1130/G25698A.1>, 2009.

762 Chew, D. M., Donelick, R. A., Donelick, M. B., Kamber, B. S., & Stock, M. J.: Apatite Chlorine Concentration
763 Measurements by LA-ICP-MS, *Geostandards and Geoanalytical Research*, 38(1), 23–35,
764 <https://doi.org/10.1111/j.1751-908x.2013.00246.x>, 2014.

765 Cogné, N., Chew, D. M., Donelick, R. A., & Ansberque, C.: LA-ICP-MS apatite fission track dating: A practical zeta-
766 based approach, *Chemical Geology*, 531, 119302, <https://doi.org/10.1016/j.chemgeo.2019.119302>, 2020.

767 Danišik, M., Shane, P., Schmitt, A. K., Hogg, A., Santos, G. M., Storm, S., Evans, N. J., Fifield, L. K., Lindsay, J. M.:
768 Re-anchoring the late Pleistocene tephrochronology of New Zealand based on concordant radiocarbon ages and
769 combined $^{238}\text{U}/^{230}\text{Th}$ disequilibrium and (U–Th)/He zircon ages, *Earth and Planetary Science Letters*, 349–350,
770 240–250, <https://doi.org/10.1016/j.epsl.2012.06.041>, 2012.

771 Donelick, R. A., O’Sullivan, P. B., & Ketcham, R. A.: Apatite Fission-Track Analysis, *Reviews in Mineralogy and*
772 *Geochemistry*, 58(1), 49–94, <https://doi.org/10.2138/rmg.2005.58.3>, 2005.



- 773 Ehlers, T. A., Szameitat, A., Enkelmann, E., Yanites, B. J., & Woodsworth, G. J.: Identifying spatial variations in
774 glacial catchment erosion with detrital thermochronology, *Journal of Geophysical Research: Earth Surface*,
775 120(6), 1023–1039, <https://doi.org/10.1002/2014JF003432>, 2015.
- 776 Evans, N. J., McInnes, B. I. A., McDonald, B., Danišik, M., Becker, T., Vermeesch, P., Shelley, M., Marillo-Sialer,
777 E., Patterson, D. B.: An in situ technique for (U–Th–Sm)/He and U–Pb double dating, *J. Anal. At. Spectrom.*,
778 30(7), 1636–1645, <https://doi.org/10.1039/C5JA00085H>, 2015.
- 779 Farley, K. A.: Helium diffusion from apatite: General behavior as illustrated by Durango fluorapatite, *Journal of*
780 *Geophysical Research: Solid Earth*, 105(B2), 2903–2914, <https://doi.org/10.1029/1999jb900348>, 2000.
- 781 Glotzbach, C., & Ehlers, T. A.: Interpreting cooling dates and histories from laser ablation in situ (U–Th–Sm)/He
782 thermochronometry: a modelling perspective, *Geochronology*, 6(4), 697–717, [https://doi.org/10.5194/gchron-6-](https://doi.org/10.5194/gchron-6-697-2024)
783 [697-2024](https://doi.org/10.5194/gchron-6-697-2024), 2024.
- 784 Flowers, R. M., Zeitler, P. K., Danišik, M., Reiners, P. W., Gautheron, C., Ketcham, R. A., Metcalf, J. R., Stockli, D.
785 F., Enkelmann, E., Brown, R. W.: (U–Th)/He chronology: Part 1. Data, uncertainty, and reporting, *GSA Bulletin*,
786 135(1–2), 104–136, <https://doi.org/10.1130/B36266.1>, 2023.
- 787 Hasebe, N., Barbarand, J., Jarvis, K., Carter, A., & Hurford, A. J.: Apatite fission-track chronometry using laser
788 ablation ICP-MS, *Chemical Geology*, 207(3–4), 135–145, <https://doi.org/10.1016/j.chemgeo.2004.01.007>, 2004.
- 789 Holder, R. M., Yakymchuk, C., & Viete, D. R.: Accessory Mineral Eu Anomalies in Suprasolidus Rocks: Beyond
790 Feldspar, *Geochemistry, Geophysics, Geosystems*, 21(8), e2020GC009052,
791 <https://doi.org/10.1029/2020GC009052>, 2020.
- 792 Horne, A. M., van Soest, M. C., Hodges, K. V., Tripathy-Lang, A., & Hourigan, J. K.: Integrated single crystal laser
793 ablation U/Pb and (U–Th)/He dating of detrital accessory minerals – Proof-of-concept studies of titanites and
794 zircons from the Fish Canyon tuff, *Geochimica et Cosmochimica Acta*, 178, 106–123,
795 <https://doi.org/10.1016/j.gca.2015.11.044>, 2016.
- 796 Horne, A. M., van Soest, M. C., & Hodges, K. V.: U/Pb and (U–Th)/He “double” dating of detrital apatite by laser
797 ablation: A critical evaluation, *Chemical Geology*, 506, 40–50, <https://doi.org/10.1016/j.chemgeo.2018.12.004>,
798 2019.
- 799 Iwano, H., Danhara, T., Danhara, Y., Hirabayashi, S., Nakajima, T., Sakai, H., & Hirata, T.: Zircon fission-track and
800 U–Pb double dating using femtosecond laser ablation–inductively coupled plasma–mass spectrometry: A
801 technical note, *Island Arc*, 29(1), <https://doi.org/10.1111/iar.12348>, 2020.
- 802 Jochum, K. P., Weis, U., Stoll, B., Kuzmin, D., Yang, Q., Raczek, I., Jacob, D. E., Stracke, A., Birbaum, K., Frick, D.
803 A., Günther, D., Enzweiler, J.: Determination of Reference Values for NIST SRM 610–617 Glasses Following
804 ISO Guidelines, *Geostandards and Geoanalytical Research*, 35(4), 397–429, [https://doi.org/10.1111/j.1751-](https://doi.org/10.1111/j.1751-908x.2011.00120.x)
805 [908x.2011.00120.x](https://doi.org/10.1111/j.1751-908x.2011.00120.x), 2011.
- 806 Ketcham, R. A., Donelick, R. A., & Carlson, W. D.: Variability of apatite fission-track annealing kinetics: III.
807 Extrapolation to geological time scales, *American Mineralogist*, 84(9), 1235–1255, [https://doi.org/10.2138/am-](https://doi.org/10.2138/am-1999-0903)
808 [1999-0903](https://doi.org/10.2138/am-1999-0903), 1999.



- 809 Ketcham, R. A.: Forward and Inverse Modeling of Low-Temperature Thermochronometry Data, *Reviews in*
810 *Mineralogy and Geochemistry*, 58(1), 275–314, <https://doi.org/10.2138/rmg.2005.58.11>, 2005.
- 811 Ketcham, R. A., Carter, A., Donelick, R. A., Barbarand, J., & Hurford, A. J.: Improved modeling of fission-track
812 annealing in apatite, *American Mineralogist*, 92(5–6), 799–810, <https://doi.org/10.2138/am.2007.2281>, 2007.
- 813 Kreuzer, H., & Harre, W.: K/Ar-Altersbestimmung an Hornblenden und Biotiten des Kristallinen Odenwaldes,
814 *Aufschluss*, 27, 71–77, 1975.
- 815 Larsen, R. B.: The distribution of rare-earth elements in K-feldspar as an indicator of petrogenetic processes in granitic
816 pegmatites: examples from two pegmatite fields in southern Norway, *The Canadian Mineralogist*, 40, 137–151,
817 2002.
- 818 Lenz, O. K., Wilde, V., Mertz, D. F., & Riegel, W.: New palynology-based astronomical and revised $^{40}\text{Ar}/^{39}\text{Ar}$ ages
819 for the Eocene maar lake of Messel (Germany), *International Journal of Earth Sciences*, 104, 873–889,
820 <https://doi.org/10.1007/s00531-014-1126-2>, 2014.
- 821 Longerich, H. P., Jackson, S. E., & Gunther, D.: Laser ablation inductively coupled plasma mass spectrometric
822 transient signal data acquisition and analyte concentration calculation, *Journal of Analytical Atomic*
823 *Spectrometry*, 11, 899–904, <https://doi.org/10.1039/JA9961100899>, 1996.
- 824 Madella, A., Glotzbach, C., & Ehlers, T. A.: How many grains are needed for quantifying catchment erosion from
825 tracer thermochronology? *Geochronology*, 4(1), 177–190, <https://doi.org/10.5194/gchron-4-177-2022>, 2022.
- 826 Mezger, K., Hanson, G. N., & Bohlen, S. R.: High-precision UPb ages of metamorphic rutile: application to the
827 cooling history of high-grade terranes, *Earth and Planetary Science Letters*, 96(1–2), 106–118,
828 [https://doi.org/10.1016/0012-821x\(89\)90126-x](https://doi.org/10.1016/0012-821x(89)90126-x), 1989.
- 829 McDowell, F. W., McIntosh, W. C., & Farley, K. A.: A precise ^{40}Ar – ^{39}Ar reference age for the Durango apatite (U–
830 Th)/He and fission-track dating standard, *Chemical Geology*, 214(3–4), 249–263,
831 <https://doi.org/10.1016/j.chemgeo.2004.10.002>, 2005.
- 832 Paton, C., Woodhead, J. D., Hellstrom, J. C., Hergt, J. M., Greig, A., & Maas, R.: Improved laser ablation U-Pb zircon
833 geochronology through robust downhole fractionation correction, *Geochemistry, Geophysics, Geosystems*,
834 11(3), 2009GC002618, <https://doi.org/10.1029/2009GC002618>, 2010.
- 835 Paul, A. N., Spikings, R. A., Chew, D. & Daly, J. S.: The effect of intro-crystal uranium zonation on apatite U-Pb
836 thermochronology: A combined ID-TIMS and LA-MC-ICP-MS study, *Geochimica et Cosmochimica Acta*, 251,
837 15–35, <https://doi.org/10.1016/j.gca.2019.02.013>, 2019.
- 838 Paul, A. N., Spikings, R. A., & Gaynor, S. P.: U-Pb ID-TIMS reference ages and initial Pb isotope compositions for
839 Durango and Wilberforce apatites, *Chemical Geology*, 586, 120604,
840 <https://doi.org/10.1016/j.chemgeo.2021.120604>, 2021.
- 841 Pickering, J., Matthews, W., Enkelmann, E., Guest, B., Sykes, C., & Kobliger, B. M.: Laser ablation (U-Th)/He
842 dating of detrital apatite, *Chemical Geology*, 548, 119683, <https://doi.org/10.1016/j.chemgeo.2020.119683>,
843 2020.



- 844 Pujols, E. J., & Stockli, D. F.: Zircon (U-Th)/(He-Pb) double-dating constraints on the interplay between thrust
845 deformation and foreland basin architecture, Sevier foreland basin, Utah, *Geosphere*, 17(6), 1890-1913,
846 <https://doi.org/10.1130/GES02372.1>, 2021.
- 847 Reiners, P. W., Campbell, I. H., Nicolescu, S., Allen, C. M., Hourigan, J. K., Garver, J. I., Mattinson, J. M., Cowan,
848 D. S.: (U-Th)/(He-Pb) double dating of detrital zircons, *American Journal of Science*, 305(4), 259-311,
849 <https://doi.org/10.2475/ajs.305.4.259>, 2005.
- 850 Schmitt, A. K., Marks, M., Nebor, A. W., & Markl, G.: The onset and origin of differential Rhine Graben volcanism
851 based on U-Pb ages and oxygen isotopic composition of zircon, *European Journal of Mineralogy*, 19(6), 849-
852 857, DOI: 10.1127/0935-1221/2007/0019-1776, 2007.
- 853 Stacey, J. S., & Kramers, J. D.: Approximation of terrestrial lead isotope evolution by a two-stage model, *Earth and*
854 *Planetary Science Letters*, 26, 207-221, 1975.
- 855 Stein, E., & Dietl, C.: Hornblende thermobarometry of granitoids from the Central Odenwald (Germany) and their
856 implications for the geotectonic development of the Odenwald, *Mineralogy and Petrology*, 72, 185-207, 2001.
- 857 Stock, G. M., Ehlers, T. A., & Farley, K. A.: Where does sediment come from? Quantifying catchment erosion with
858 detrital apatite (U-Th)/He thermochronometry, *Geology*, 34(9), 725-728, <https://doi.org/10.1130/G22592.1>,
859 2006.
- 860 Tripathy-Lang, A., Hodges, K. V., Monteleone, B. D., & van Soest, M. C.: Laser (U-Th)/He thermochronology of
861 detrital zircons as a tool for studying surface processes in modern catchments, *Journal of Geophysical Research:*
862 *Earth Surface*, 118(3), 1333-1341, <https://doi.org/10.1002/jgrf.20091>, 2013.
- 863 Wagner, G. A.: Spuren der spontanen Kernspaltung des ²³⁸Urans als Mittel der Datierung von Apatiten und ein Beitrag
864 zur Geochronologie des Odenwaldes, *N. Jb. Miner. Abh.*, 110(3), 252-286, 1969.
- 865 Will, T. M., Schmädicke, E., Ling, X.-X., Li, X.-H., & Li, Q.-L.: Geochronology, geochemistry and tectonic
866 implications of Variscan granitic and dioritic rocks from the Odenwald-Spessart basement, Germany, *Lithos*,
867 404-405, 106454, <https://doi.org/10.1016/j.lithos.2021.106454>, 2021.
- 868 Williams, I. S.: U-Th-Pb geochronology by ion microprobe. In: McKibben, M.A., Shanks III, W.C., Ridley, W.I.
869 (Eds.), *Applications of microanalytical techniques to understanding mineralizing processes*, *Reviews in*
870 *Economic Geology*, 7, 1-35, 1998.
- 871 Zattin, M., Andreucci, B., Thomson, S. N., Reiners, P. W., & Talarico, F. M.: New constraints on the provenance of
872 the ANDRILL AND-2A succession (western Ross Sea, Antarctica) from apatite triple dating: APATITE
873 TRIPLE DATING IN ANTARCTICA, *Geochemistry, Geophysics, Geosystems*, 13(10),
874 <https://doi.org/10.1029/2012GC004357>, 2012.
- 875 Ziegler, P. A.: *Geological Atlas of Western and Central Europe*, 239 pp., Shell Int. Pet. Maatschappij, Geol. Soc.
876 Publ. House, Bath, UK, 1990.
- 877